

1      **Implementation of WRF-Urban Asymmetric Convective Model (UACM) for**  
2      **Simulating Urban Fog over Delhi, India**

4      **Utkarsh Prakash Bhautmage<sup>1\*</sup>, Sachin D. Ghude<sup>1\*</sup>, Avinash N. Parde<sup>1,2</sup>, Harsh G. Kamath<sup>5</sup>,**  
5      **Narendra Gokul Dhangar<sup>1</sup>, Jonathan Pleim<sup>3</sup>, Michael Mau Fung Wong<sup>4</sup>, Sandeep Wagh<sup>1</sup>,**  
6      **Rakesh Kumar<sup>6</sup>, Dev Niyogi<sup>5</sup>, M. Rajeevan<sup>7</sup>**

7  
8      <sup>1</sup>Indian Institute of Tropical Meteorology, Ministry of Earth Sciences (MoES), Pashan, Pune,  
9      India.

10     <sup>2</sup>Department Atmospheric and Space Sciences, Savitribai Phule Pune University, Pune, India.

11     <sup>3</sup>Atmospheric & Environmental Systems Modeling Division, CEMM/ORD/USEPA, Research  
12     Triangle Park, NC, USA.

13     <sup>4</sup>Division of Environment and Sustainability, Hong Kong University of Science and Technology,  
14     Hong Kong, China.

15     <sup>5</sup>Department of Earth and Planetary Sciences, Jackson School of Geosciences, The University of  
16     Texas at Austin, Austin, TX 78712, USA.

17     <sup>6</sup>India Meteorological Department, New Delhi, India.

18     <sup>7</sup>Ministry of Earth Sciences, New Delhi, India.

19  
20  
21     \*Corresponding authors: Utkarsh Prakash Bhautmage ([upbhaut mage@connect.ust.hk](mailto:upbhaut mage@connect.ust.hk)),  
22                                Sachin D. Ghude ([sachin ghude@tropmet.res.in](mailto:sachin ghude@tropmet.res.in))

23  
24     † Indian Institute of Tropical Meteorology, Pashan, Pune, India.  
25  
26

27      **Key Points:**

- 28     1. The new multilayer WRF-UACM, explicitly incorporating urban physics and morphology, is  
29        implemented to simulate fog over the Delhi region.  
30     2. Improvements in the prediction of urban wind, temperature, and relative humidity are  
31        demonstrated using UACM on fog days and clear skies.  
32     3. Abilities of novel UACM in capturing urban fog phenomena along with its operational mode  
33        capabilities over the Delhi region are examined.

34 **Abstract**

35 Accurate fog prediction in densely urbanized cities poses a challenge due to the complex  
36 influence of urban morphology on meteorological conditions in the urban roughness sublayer.  
37 This study implemented a coupled WRF-Urban Asymmetric Convective Model (WRF-UACM)  
38 for Delhi, India, integrating explicit urban physics with Sentinel-updated USGS land-use and  
39 urban morphological parameters derived from the UT-GLOBUS dataset. When evaluated against  
40 the baseline Asymmetric Convective Model (WRF-BACM) using Winter Fog Experiment  
41 (WiFEX) data, WRF-UACM significantly improved urban meteorological variables like diurnal  
42 variation of 10-meter wind speed, 2-meter air temperature (T2), and 2-meter relative humidity  
43 (RH2) on a fog day. UACM also demonstrates improved accuracy in simulating temperature and  
44 a significant reduction in biases for RH2 and wind speed under clear sky conditions. UACM  
45 reproduced the nighttime urban heat island effect within the city, showing realistic diurnal  
46 heating and cooling patterns that are important for accurate fog onset and duration. UACM  
47 effectively predicts the onset, evolution, and dissipation of fog, aligning well with observed data  
48 and satellite imagery. Compared to WRF-BACM, WRF-UACM reduces the cold bias soon after  
49 the sunset, thus improving the fog onset error by ~4 hours. This study underscores the UACM's  
50 potential in enhancing fog prediction, urging further exploration of various fog types and its  
51 application in operational settings, thus offering invaluable insights for preventive measures and  
52 mitigating disruptions in urban regions.

53

54

55 **Plain Language Summary**

56 In Delhi, accurately predicting fog in urban areas is difficult due to complex factors like city  
57 layout and infrastructure. This study employed the recently developed WRF-UACM with  
58 detailed UT-GLOBUS urban morphological parameters for fog simulation. Compared to existing  
59 models, WRF-UACM predicted wind, temperature, and humidity better under both clear skies  
60 and foggy conditions. Our model accurately reproduced urban warming and cooling patterns that  
61 are crucial for fog prediction and urban meteorology. WRF-UACM improves the diurnal  
62 variation of winds and reduces temperature cold bias after the sunset, thus improving fog onset  
63 by ~4 hours. This work highlights the potential of WRF-UACM for fog prediction and offers  
64 valuable insights for urban meteorology.

65

66

67 **Keywords:**

68 Boundary layer meteorology, Urban canopy parameterization, Urban morphological parameters,  
69 Urban heat island, WRF model, Fog

70

71     **1. Introduction**

72       In the densely populated Indo-Gangetic Plains (IGP), the winter season ushers in frequent  
73       and widespread fog occurrences (Bhushan et al., 2003; Singh and Kant, 2006; Gautam et al.,  
74       2007; Ghude et al., 2017). These fog episodes drastically reduce visibility to just a few tens of  
75       meters, disrupting transportation and impacting the lives of millions of inhabitants. Radiation  
76       fog, a prevalent type in this region (Singh and Kant, 2006; Singh et al. 2007; Ghude et al.,  
77       2023), has exhibited significant spatiotemporal variability due to the complex terrain of the area,  
78       including urbanization over the past two decades (Sawaisarje et al., 2014; Singh and Gautam,  
79       2022; Parde et al., 2023). Rapid urbanization leads to changes in local climate and conducive  
80       fog meteorology, resulting in "urban fog" (Sachweh and Koepke, 1997). Urbanization disrupts  
81       natural temperature, humidity, aerosol loading and wind circulation, leading to the genesis of an  
82       "urban heat island" (UHI) that is often characterized by higher land surface and air temperatures  
83       in cities compared to surrounding rural areas (AMS Glossary, 2020). As urban areas in the IGP,  
84       particularly Delhi region, continue to sprawl, there is a corresponding rise in the occurrence of  
85       fog "holes" or patches that tend to dissipate at an earlier stage (Gautam & Singh, 2018).  
86       Considering the future, climate change could lead to more frequent episodes of widespread fog  
87       over the IGP in winter, except in areas where air pollution and greenhouse warming effects  
88       outweigh the fog formation (Hingmire et al., 2021). Recent research by Gu et al. (2019) and  
89       Hingmire et al. (2021) has revealed a decrease in fog events over urbanized regions of Shanghai  
90       and the North India over the past recent years. This decline is mainly attributed to the urban heat  
91       island (UHI) effect resulting from changes in land use and surface properties. Gautam and Singh  
92       (2018) and other sources have reported that the UHI effect leads to higher surface temperatures  
93       and reduced relative humidity, resulting in decreased condensation and, consequently, reduced  
94       fog formation.

95       Globally, radiation fog events, including those in Delhi, pose challenges for Numerical  
96       Weather Prediction (NWP) models to simulate and predict (Pithani et al., 2020; Jaykumar et al.,  
97       2021; Parde et al., 2022a). Various factors contribute to the complexity of fog, including the  
98       boundary layer phenomenon, which may involve interactions between air masses with different  
99       temperatures and moisture content, meteorological field-variables' variations, interactions  
100      between atmospheric flow and complex landscapes, large-scale synoptic motions, and the impact

of aerosol loading in the shallow boundary layer (Bhowmik et al., 2004; Jenamani et al., 2007; Sawaisarje et al., 2014; Ghude et al., 2017, 2023; Hingmire et al., 2019; Dhangar et al., 2021, 2022; Gunturu and Kumar, 2021). Accurately predicting fog through the present numerical models remains a formidable challenge. Typically, individual model forecasts tend to exhibit a noticeable bias in the onset and dissipation timing of fog (Bhowmik et al., 2004; Jayakumar et al., 2018; Pithani et al., 2020; Wagh et al., 2023; Yadav et al., 2022). However, a recently introduced ensemble fog forecasting approach (utilizing the ensembles of multiple initial conditions or models or physics) proves to be more effective than single-model-based forecasts in addressing the biases related to fog onset and dissipation (Zhou and Du, 2010; Price et al., 2015; Pahlavan et al., 2021; Parde et al., 2022a). Nevertheless, it's important to note that this ensemble-based approach comes with increased computational costs. While data assimilation has the potential to address several issues in fog forecasting that stem from errors in the initial conditions of land-surface fields (e.g. soil moisture and temperature) and atmospheric states, persistent challenges remain within the models for fog prediction, including large onset errors, diurnal bias in 2-meter temperature due to rapid warming(cooling) during day(night), in 10-meter wind speed, and over-prediction of liquid water content (LWC) within the fog layers as well as bias in their vertical extents (Bari et al., 2023; Bergot and Guedalia, 1994; Ghude et al., 2023; Müller et al., 2007; Rémy et al., 2010; Steeneveld et al., 2015; Gao et al., 2018; Pithani et al., 2020; Parde et al., 2022b). Furthermore, urban warming frequently disrupts boundary layer stability, the inversion layer, and diminishes liquid droplets due to reduced condensation in urban locales, thereby hindering the genesis of radiation fog (Gu et al., 2019). The large-eddy simulation study at Paris–Charles de Gaulle airport by Bergot et al. (2015) emphasizes the critical importance of incorporating comprehensive building representations to enhance the precision of local radiation fog forecasts. This underscores the necessity of considering small-scale variations within the urban canopy to advance the accuracy of fog predictions. However, the presently available operational fog forecasting models, especially in India, lack consideration for detailed urban morphology representation and realistic UHI effect. This has resulted in reduced forecasting accuracy and an increased likelihood of false alarm ratio (Pithani et al., 2020; Parde et al., 2022a). In essence, these investigations highlight the significance of adopting advanced numerical modeling methods to inform efficient fog adaptation strategies in cities.

The study conducted by Theethai Jacob et al. (2023) involved the integration of a comprehensive urban surface-flux scheme into a high-resolution Delhi Model with Chemistry and aerosol framework (DM-Chem), utilizing urban morphology data specific to the Delhi region obtained from empirical relationships. Their aim was to simulate the UHI and urban cool island (UCI) effects under clear sky and foggy conditions. However, significant biases were identified in the simulation of relative humidity and the underestimation of latent heat flux, particularly during foggy conditions. For precise representation of urban boundary layer, specific urban modeling options have also been integrated into the state-of-the-art Weather Research and Forecasting (WRF) model. These include the single-layer Urban Canopy Model (UCM) (Kusaka et al., 2001), and multi-layer Building Effect Parameterization-Building Energy Model (BEP-BEM) (Martilli et al., 2002; Salamanca & Martilli, 2010). However, these urban models present certain challenges and limitations, particularly when implemented in operational mode (details elaborated in Bhautmage et al., 2022). Notably, a drawback of the renowned BEP-BEM model is its coupling with only a limited set of local planetary boundary layer (PBL) schemes in WRF such as, Mellor-Yamada-Janjic (MYJ) (Janjić, 1994; Mellor & Yamada, 1974, 1982) and Boulae (Bougeault & Lacarrere, 1989), and nonlocal Yonsei University (YSU) scheme (Hong et al., 2006; Hendricks et al., 2020). Furthermore, these models are computationally resource-intensive when operated at higher spatial, vertical, and temporal resolutions (Chen & Dudhia, 2001). Importantly, UCM and BEP-BEM models in WRF can only be coupled with the Noah and Noah-MP land surface models (Chen et al., 2011; Niu et al., 2011). To address these challenges and limitations, a recently developed Urban Asymmetric Convective Model (UACM) was introduced by Dy et al. (2019) and Bhautmage et al. (2022).

The UACM is a multilayer urban model based on a hybrid local and non-local flux PBL scheme. The model can estimate the momentum drag exerted by the building structures on the airflow as well as the thermal and moisture fluxes evolving from the urban facets. The urban morphological parameters play a vital role in simulating the meteorological conditions and field variable magnitudes within the urban roughness sublayer in the UACM. The model has shown significant improvement in simulating the wind speed and temperature when implemented over the dense-urbanized Pearl River Delta (PRD) economic region in Southern China (Bhautmage et al., 2022). The UACM demonstrates improved urban 10-meter wind speeds (WS10) by generating sufficient momentum drag, and 2-meter temperatures (T2) by considering the daytime

storage of solar thermal energy within urban structures, and its subsequent release in the nighttime. This extends to the precise modeling of vertical profiles of horizontal wind speeds and temperatures within the urban canopy layer and up to the PBL depth. The model also improves the 2-meter total moisture content and its diurnal trend in urban areas. Furthermore, UACM effectively captures the nocturnal UHI effect by efficiently releasing the daytime stored heat back into the atmosphere. In comparison to alternative urban models, UACM excels in computational efficiency, rendering it well-suited for operational forecasting. More comprehensive insights into the UACM, including its integration with the WRF Version 3.8 (V3.8) model are described in Dy et al. (2019) and Bhautmage et al. (2022).

In this study, we have implemented the WRF-UACM over the urban areas in Delhi region, aiming to simulate scenarios of both the radiation fog event and clear sky day. To enhance the model's accuracy, we have incorporated the most up-to-date United States Geological Survey (USGS) land use data over the Delhi region updated from European Space Agency (ESA) World-Cover 2021 (<https://worldcover2021.esa.int>) Sentinel satellite observations (Van De Kerchove et al., 2021) as well as high-resolution urban morphological parameters over Delhi derived from the UT-GLOBUS (Kamath et al., 2022). The article is structured as: Section 2 provides comprehensive details about the model framework, urban morphological data, observational sites and data, and case studies specifics. In Section 3, we discussed the research findings for fog and clear sky episodes from both modeling and observational perspectives. Finally, the study concludes with a summary in Section 4.

182

## 183 **2. Datasets and Methodology**

### 184 **2.1 Urban Asymmetric Convective Model (UACM) Framework**

185 In this study, the non-hydrostatic mesoscale WRF V3.8 is utilized. This model is fully  
186 compressible and utilizes a terrain-following vertical coordinate system. WRF incorporates  
187 various physics scheme options for cloud/precipitation microphysics, cumulus convection, PBL,  
188 land surface, and shortwave and longwave radiation. These options vary in complexity to  
189 accurately simulate atmospheric processes across various spatial scales and regions (Skamarock  
190 et al., 2008).

To simulate the urban boundary layer processes, the UACM (Dy et al., 2019; Bhautmage et al., 2022) within WRF has been implemented. The UACM incorporates innovative urban physics through a hybrid local and non-local flux mixing PBL scheme, seamlessly integrated with the modified Pleim-Xiu (PX) land surface model (LSM). This integration effectively addresses urban sensible and latent heat fluxes, alongside momentum fluxes. The UACM is a multilayer urban model that accommodates intricate street canyon geometry and can ingest various urban morphological parameter datasets, including street canyon orientation. All these derived morphological parameters are comprehensively explained in section 2.2. The UACM employs a two-layer force-restore algorithm to estimate urban surface temperatures across the ground, walls, and roofs. These estimations incorporate urban morphological parameters that play a vital role in estimating the amount of radiation reaching urban surfaces, accounting for canyon orientations and dynamic solar zenith angle across diurnal and seasonal cycles. Notably, the model includes momentum drag induced by all three urban surfaces (street, walls, and roof) to simulate wind velocity within the urban canopy (Bhaut mage et al., 2022).

In the present work, the WRF-UACM model was configured over the Delhi region, specifically centered on the urbanized expanse of the Delhi-National Capital Region (NCR). This is achieved through a nested configuration of domains in the WRF model as shown in Figure 1a, utilizing the reference latitude of  $28.6^{\circ}$  N and longitude of  $77.219^{\circ}$  E as the center for coarser Domain-1 (D1). Encompassing an extensive area of  $2,200,000 \text{ km}^2$ , D1 spans northern India, parts of Pakistan and Afghanistan to the west, and the western reaches of China. Domain-2 (D2) covers a more confined area of  $36,481 \text{ km}^2$ , including the Delhi region and major neighboring cities such as Gurugram, Faridabad, Ghaziabad, Greater Noida, as well as smaller urban centers like Rohtak, Sonipat, Panipat, Meerut, and Muzaffarnagar to the north. The terrain height in the Delhi urban region varies from 210 to 220 m above mean sea level (AMSL). The nested domains have a grid spacing ratio of 1:5, with different grid resolutions for each domain. D1 has a grid spacing of 5 km, while D2 has a finer resolution with a grid spacing of 1 km. The grid configurations for D1 and D2 are 440 x 200 and 191 x 191, respectively. To capture the vertical structure of the atmosphere, the model employs 54 vertical eta levels, extending up to the 50 hPa pressure height. The first seven layers are within a height of 30 meters above ground level (AGL), followed by around ten layers within 60 meters AGL, and 19 layers extending up to 1 km AGL to effectively capture the boundary layer processes. Additional details regarding the

222 various physics options and model configuration settings used in the study are provided in Table  
223 1.

224 The default United States Geological Survey (USGS)-24 category, which was created in  
225 WRF V3.8 based on the 1992-93 Global Land Cover Characterization (GLCC) data at a  
226 resolution of 30 arc-seconds, has become obsolete and inadequate for accurately representing  
227 urban classification within and around urban regions like Delhi. Therefore, in the present study,  
228 the land use land cover (LULC) has been updated entirely over the Delhi region (Figure 1b)  
229 using the recently released (October 28, 2022) European Space Agency (ESA) World-Cover  
230 2021 data (<https://worldcover2021.esa.int>). This dataset boasts a higher resolution of 10 m. The  
231 updated dataset is derived from data furnished by Sentinel-1 (Synthetic Aperture Radar) and  
232 Sentinel-2 (High-Resolution Optical Earth Observation Data) satellites. It was made public on  
233 October 28, 2022, and demonstrates an overall global accuracy of 76.7% (Van De Kerchove et  
234 al., 2021). The updated LULC, obtained by resampling the ESA data at a resolution of 30 arc-sec  
235 (~1 km), exhibits good agreement with the actual urban distribution observed in satellite images.  
236 This agreement extends to other categories present in the region covered by D2 (Figure 1c). The  
237 elevation in domain D2 is approximately 300 m AMSL, with irrigated cropland being dominant  
238 in the northeast. The remaining area encompasses dryland, shrubland, and water bodies.

239

## 240 **2.2 Urban Morphological Parameters Datasets**

241 To implement the coupled WRF-UACM model over Delhi region, urban morphological  
242 parameters have been considered. These parameters include average building height ( $H$ ), plan  
243 area density ( $\lambda_p$ ), frontal area density ( $\lambda_f$ ), and street canyon orientation ( $\varphi$ ). These parameters  
244 have been meticulously developed for the Delhi region (shown in Figure 2), attributed to each 1  
245 km<sup>2</sup> urban grid cell in D2, utilizing the methodology described in Bhautmage et al. (2022). In  
246 deriving the first three parameters, the building polygon shapefile of the UT-GLOBUS dataset  
247 (Kamath et al., 2022) has been employed in conjunction with embedded building height data  
248 pertinent to the Delhi region. Evidently, the  $H$  ranges from ~8 to 10 m across the region,  
249 escalating to 12 to 14 m within densely populated sectors. On the outskirts of the city,  $\lambda_p$  is ~0.1,  
250 and in the inner regions it is ~0.4 with some areas reaching a maximum density of 0.8 in  
251 extremely dense regions. Within the inner city,  $\lambda_f$  varies from 0.4 to 0.6, surpassing 1.0 in  
252 regions marked by extensive urbanization. The urban grid cells in D2 for which there are no

253 urban morphological parameters data available, default values of 6 m, 0.45, and 0.45 have been  
254 assumed for  $H$ ,  $\lambda_p$ , and  $\lambda_f$ , respectively.

255 From these parameters data, the generalized information of street canyon width ( $W$ ) and  
256 building width ( $B$ ) can be obtained to ingest the urban geometry in a repeating canyon form into  
257 the model. Additionally, the requisite values of other parameters like sky view factors for road  
258 ( $\psi_r$ ) and walls ( $\psi_w$ ) for each urban grid cell, are also estimated based on the canyon dimensions  
259 ( $H, W$ ) following the methodology in Masson (2000). The street canyon orientation parameter  
260 ( $\varphi$ ) data, which represents the dominant street angle at which the majority of streets are aligned,  
261 is obtained for each urban grid cell by processing the street-map shapefile of the Delhi region  
262 (Geofabrik, 2018) obtained from <https://www.geofabrik.de/data/download.html> in the Geographic  
263 Information System (GIS) software. Employing a length weighting approach, emphasis is  
264 accorded to longer street canyon lengths. Predominantly, the canyon orientation within Delhi city  
265 adheres to the north-south direction, while less densely populated outskirts exhibit an east-west  
266 orientation.

267

## 268 **2.3 Observational Sites and Datasets**

269 To evaluate the performance of the WRF-UACM over the Delhi region, meteorological  
270 observations from ground-based stations are used. These stations (depicted in Figure 1d) are  
271 strategically positioned in urban areas, covering areas with low, mid, and high urban  
272 development. Specifically, the Delhi University, Akshardham, and Pitampura stations reside  
273 within densely populated urban regions, while Narela, Mungeshpur, Jafarpur, and Ayanagar  
274 stations are situated on the outskirts of Delhi, encompassing less densely populated areas.  
275 Frequent fog episodes having wide-spread nature occur during the winter season in the IGP  
276 region, often resulting in reduced visibility below 1 km and sometimes few tens of meters (very  
277 dense fog events). Consequently, to gain insights into the fog genesis, lifecycle, and mechanisms  
278 behind the spatiotemporal variations, the Winter Fog Experiment (WiFEX; Ghude et al., 2017)  
279 field campaigns have been conducted at the Indira Gandhi International Airport (IGIA) site  
280 (28.56 °N, 77.09 °E, 216 m AMSL) in New Delhi. The WiFEX campaigns have taken place  
281 during the winter season (December-February) since 2015 (Ghude et al., 2023, 2017). For the  
282 present study, observation data from the 2017-18 WiFEX campaign at the IGIA site were also  
283 utilized to evaluate the model performance.

284       The observation data used for model verification include measurements of relative  
285       humidity (RH) and air temperature (T) measured at a height of 2-meters. These measurements  
286       were obtained using a T and RH sensor (HMP45C Vaisala Oyj, Finland) installed on a 20-meter  
287       tower, with a temporal sampling frequency of 1-minute. Wind Speed (WS) data at a height of 10-  
288       meter were obtained using multicomponent weather sensors (WXT 520, Vaisala Oyj, Finland)  
289       installed on the same 20-meter tower with a temporal sampling frequency of 1-minute.  
290       Additionally, apart from the IGIA site data, meteorological data from other stations, including  
291       the radiosonde profile data at Ayanagar (which provides vertical profiles of wind speed,  
292       temperature, and humidity), were obtained from the Indian Meteorological Department (IMD,  
293       Delhi). All meteorological data collected at a higher temporal sampling frequency of 1-minute  
294       were subsequently aggregated over hourly periods for model verification purposes.

295

## 296       **2.4 Case Studies and Model Simulation Details**

297       Two cases have been identified to evaluate the performance of the model. The first case  
298       pertains to a dense radiation fog event that occurred on January 29-30, 2017. Throughout this  
299       period, the prevailing wind direction over the IGP region was predominantly westerly and north-  
300       westerly. Prior to the onset of the fog at IGIA, the wind conditions were calm (wind speed less  
301       than  $2 \text{ m s}^{-1}$ ), indicating minimal wind movements. The onset of fog was at 00:00 local time  
302       (IST-Indian Standard Time) on January 30<sup>th</sup> (18:30 UTC on 29 January) and dissipated  
303       completely by the morning of the same day at 11:00 IST, thus sustaining the fog for a total of 11  
304       hours. The fog was determined by a visibility threshold of 1000 meters. Notably, during this  
305       event, the visibility at the IGIA site reached its lowest point, dropping to around 92 meters at  
306       05:00 IST on January 30<sup>th</sup>, 2017. This case has been selected to evaluate the model's  
307       performance in accurately capturing the characteristics and dynamics of the radiation fog event,  
308       including visibility conditions.

309       The second case selected for assessing the UACM model performance involves clear sky  
310       conditions (no-fog case) from December 20-22, 2016. During this period, the prevailing winds  
311       also originated from the west and northwest, however, the wind speeds were higher ( $> 2.0 \text{ m s}^{-1}$ )  
312       compared to the fog episode. Analysis of the WiFEX (2015-16) campaign (Ghude et al., 2017)  
313       data revealed that the RH remained below 80%, cloud cover was less than 25%, and visibility  
314       consistently exceeded 2000 meters throughout the entire period. This case has been selected to

315 examine the model's ability to accurately reproduce meteorological conditions in scenarios  
316 characterized by clear skies, the absence of clouds and rainfall, and the presence of abundant  
317 sunshine.

318 For both the selected cases, the model simulations were conducted by performing a  
319 model spin-up process for both the baseline WRF-BACM (WRF-Base Asymmetric Convective  
320 Model, WRF V3.8 model control runs with the default existing base PX-LSM and base ACM2-  
321 PBL scheme, and without using any other existing explicit urban modeling option and urban  
322 morphological parameters dataset) and WRF-UACM. The fog-event model-run was initialized  
323 on January 29, 2017, at 00:00 UTC, with a 6-hour spin-up time to ensure the model reached a  
324 stable state at least 18 hours before the onset of fog. Similarly, the clear sky case was initialized  
325 on December 19, 2016, at 00:00 UTC, with a same spin-up period to establish model stability  
326 before the actual simulation analysis time began.

327 Typically, when simulations are conducted for regional weather forecasting using the  
328 WRF model, the minimum required input data includes the initial and boundary meteorological  
329 conditions for all nested domains, as well as land-use category data specifying fractions for  
330 urban, vegetation, and other categories. Additional useful data encompassed detailed soil and  
331 vegetation classification categories, along with their corresponding thermal and hydraulic  
332 properties. The initial and boundary meteorological conditions for the simulations are acquired  
333 from the National Centers for Environmental Prediction (NCEP) final analysis (FNL) data. This  
334 dataset is produced by conducting global forecast system simulations using observations from  
335 around the globe. The selected NCEP data has a spatial resolution of  $1^{\circ}$  in both latitude and  
336 longitude, and a temporal resolution of 6 hours. The updated USGS-Sentinel land use data is  
337 utilized for both WRF-BACM and WRF-UACM simulations. However, the WRF-UACM runs  
338 require additional urban morphological parameters such as average building height ( $H$ ), plan area  
339 density ( $\lambda_p$ ), frontal area density ( $\lambda_f$ ), and street canyon orientation ( $\varphi$ ).  
340

### 341 **3. Results and Discussion**

342 In this section, the UACM's performance is meticulously assessed across both case  
343 studies discussed in Section 2.4, offering a comprehensive presentation of detailed comparisons  
344 and result analysis together with the BACM model. A profound understanding of the simulations  
345 for each case emerges through spatial plots showcasing model discrepancies between the UACM

346 and BACM across T2, RH2, LWC and WS10. Furthermore, spatial plots of UACM-simulated  
347 surface LWC during the fog dissipation hours are presented, along with a comparison to NASA's  
348 MODIS satellite image taken around 10:30 am IST. These comparisons highlight the UACM's  
349 ability to capture fog dynamics and the burn-off mechanism during the dissipation over the  
350 urbanized Delhi region. Time-series analysis of the bias (Model – Observation) for T2, RH2 and  
351 WS10 is conducted at various meteorological stations in the urban region of Delhi-NCR.  
352 Additionally, comparison of modeled results for the vertical profiles of RH, potential  
353 temperature ( $\theta$ ), and WS were made using the radiosonde data collected at the Ayanagar station.  
354 Overall, this analysis provides insights into the performance of the UACM and its skill in  
355 simulating urban fog characteristics. Similarly, the UACM's competence in replicating  
356 meteorological conditions during clear sky events is also analyzed. The focus of this assessment  
357 is to evaluate how accurately the UACM represents crucial meteorological variables such as  
358 temperature, humidity, and wind speed during periods characterized by clear sky conditions.

359

### 360 **3.1 Fog Case (January 29-30, 2017)**

361 Figures 3(a-d), 3(e-h), 3(i-j), and 3(m-p) present the model differences between UACM  
362 and BACM for near surface T2, RH2, LWC, and WS10 variables, respectively, at key timings:  
363 21:00 IST (15:30 UTC, 29-Jan), 03:00 IST (21:30 UTC, 29-Jan), 06:00 IST (00:30 UTC, 30-  
364 Jan), and 09:00 IST (03:30 UTC, 30-Jan). These time intervals correspond to the stages before,  
365 during, mature, and the posterior fog conditions. The BACM model simulates much lower urban  
366 temperatures compared to UACM caused by a rapid drop in temperature after sunset over the  
367 Delhi-NCR region as shown in Figure 3a. The absence of the UHI effect in the BACM leads to a  
368 rapid cooling in nocturnal temperatures, which further contributes to the steep increase in RH2  
369 and LWC. Moreover, the adjacent regions surrounding the city area also display enhanced levels  
370 of LWC in the BACM simulation (Figure 3i and 3j). This shift in LWC patterns from actual  
371 observations can be ascribed to their marginally lower temperatures and the windy conditions,  
372 including the influence of rural-urban breezes. These breezes facilitate the augmented influx of  
373 moisture from nearby sources such as irrigated croplands and the Yamuna River that flows  
374 through the city.

375 The UACM, on the other hand, proficiently captures the nocturnal UHI effect,  
376 demonstrating its efficacy in simulating temperature variations and urban climate characteristics

377 in comparison to the BACM. The UACM manifests higher T2 at 21:00 IST on 29 January and  
378 03:00 IST on 30 January (Figure S3 in the supporting information). This higher temperature is  
379 attributed to the release of daytime stored heat in the urban infrastructure back into the  
380 atmosphere and limited sky-view from the street which reduces radiative cooling. The impact of  
381 UACM on LWC is particularly evident over urban areas during the nighttime fog period as  
382 shown in Figures 3(i-k). This decrease in LWC is most pronounced before the onset of fog at  
383 21:00 IST, revealing the UACM's ability to effectively reduce LWC.

384 The reduction in the magnitudes of wind speed by 0.5-2.0 m s<sup>-1</sup> over the urban region in  
385 the UACM compared to the BACM as shown in Figures 3(m-p) is mainly attributed to the  
386 momentum drag resulting from the explicit inclusion of urban structures in the model. Urban  
387 morphological parameters like building heights, frontal area, and street orientation significantly  
388 contribute to the reduction in wind speed within urban domains (More details can be found in  
389 Figures S1, S2, and S5 in the supporting information).

390 In Figures 4(a-b), spatial plots illustrate the UACM-simulated near-surface LWC at 10:00  
391 IST and 11:00 IST, while Figure 4c presents NASA's MODIS sensor-captured satellite image  
392 around ~10:30 IST in the morning. The MODIS image clearly depicts the burn-off (dissipation)  
393 of fog layers over the urban areas including Delhi, forming a clear area or "hole" within the city,  
394 while the fog persists in the surrounding areas. The UACM simulation shows low LWC values  
395 over the urbanized areas at both 10:00 IST and 11:00 IST, aligning well with the spatial pattern  
396 observed in the MODIS satellite image. This agreement between the UACM simulation and the  
397 satellite image indicates the model's ability to capture the fog burn-off process and the influence  
398 of urban heat release on dissipating fog over urban areas.

399 Figures 5(a-c) present time-series plots depicting the bias between modeled data and  
400 observations for T2, RH2, and WS10, respectively, at six stations in Delhi-NCR. The bold lines  
401 in the plots represent the bias of UACM values compared to the observations, while the dashed  
402 lines indicate the bias exhibited by the BACM. Positive values indicate over-prediction, whereas  
403 negative values indicate under-prediction. Notably, the UACM excels during the fog period  
404 (from 29-Jan-2017, 23:00 IST to 30-Jan-2017, 11:00 IST), closely aligning with observed  
405 conditions. The UACM reduced overestimation of daytime T2 compared to BACM by  
406 generating a cooling effect due to the combined influence of urban structures and the solar zenith  
407 angle. The model also released daytime stored heat during nighttime hours, resulting in warmer

408 temperatures compared to the BACM. Particularly noteworthy is the UACM accurately  
409 simulating the nighttime UHI effect. The diurnal trend of RH2 is also effectively captured by the  
410 UACM as seen in Figure 5b, thus reducing bias. While UACM slightly underestimates RH2  
411 before the night of fog onset, it demonstrates improvement the following day post-event. Lastly,  
412 the UACM significantly improved the prediction of WS10 at Delhi stations, closely aligning  
413 with observed data (Figure 5c). This reduction in bias indicates the UACM's ability to simulate  
414 wind patterns within the urban canopy. During fog episodes, the UACM adeptly reproduces calm  
415 wind conditions, effectively modeling meteorological aspects of fog events, such as low wind  
416 speeds under stable atmospheric conditions. Overall, the UACM proficiently reproduces fog  
417 event meteorology, leading to improved predictions for T2, RH2, and WS10 compared to the  
418 BACM.

419 Figure 5d illustrates the time-series comparison of LWC predicted by BACM and UACM  
420 models, alongside observed horizontal visibility at IGIA. UACM consistently simulates lower  
421 LWC values ( $0\text{--}0.4 \text{ g m}^{-3}$ ) due to liquid droplet evaporation from higher temperatures and air  
422 remaining away from saturation point in urban regions. The UACM demonstrates a significant  
423 improvement in fog forecasting compared to the BACM, as evidenced from improvement in the  
424 fog onset time prediction by a delay of approximately 3 hours in the predicted LWC values. The  
425 onset of fog, indicated by visibility dropping below 1000 m (moderate fog conditions), aligns  
426 well with the UACM's delayed LWC prediction. As the LWC values rise and reach their peak,  
427 visibility starts dropping below 500 m, indicating the presence of dense fog. During the period of  
428 dense fog (04:00 IST - 09:00 IST, 30 January), the UACM simulates LWC values ranging from  
429 0.1 to  $0.3 \text{ g m}^{-3}$  with visibility declining to around 92 m at 05:00 IST on 30 January. In addition,  
430 the UACM demonstrates an early dissipation of fog compared to the BACM, resulting in the  
431 formation of clear areas or "holes" over urban regions due to the burned-off mechanism. During  
432 the dissipation phase of the fog after sunrise, the solar radiation reaching the ground surface  
433 intensifies in the morning hours and the surface temperature as well as the temperature in the  
434 boundary layer starts to rise. This triggers instability leading to an augmentation of vertical  
435 turbulent mixing and a concurrent reduction in RH near the surface. This phenomenon aligns  
436 well with the gradual increase in visibility observed at the IGIA site after sunrise (Figure 5d).  
437 When considering fog occurrences, the temporal variation of LWC from the WRF-UACM model  
438 closely matches the LWC profiles derived from microwave radiometer (MWR) observations

439 (visibility dropping below 500 m) at IGIA (Figurer 5e). It is noteworthy, that the model-derived  
440 LWC in Pithani et al., (2020) consistently exhibit an overestimation of LWC values when  
441 compared to the actual observations, thus falling short in accurately representing the true fog  
442 intensity. The implementation of the WRF-UACM led to a reduction in the overestimation of  
443 LWC values as observed in this study. The UACM's simulation of fog dissipation and the  
444 corresponding improvement in visibility corroborate its ability to capture the dynamic nature of  
445 fog events in the study area.

446 During a fog episode, the UACM performance is better than BACM, particularly for the  
447 WS10, T2, and RH2 with index of agreement (IOA) of 0.89, 0.96, and 0.92, respectively. Mean  
448 bias (MB) and Mean error (ME) are reduced to 0.14 and  $0.36 \text{ m s}^{-1}$  by the UACM for WS10 (i.e.,  
449 73.07% and 47.8% improvement, respectively). Similarly, normalized mean bias (NMB) is  
450 reduced by 29% and normalized mean error (NME) by 24% for WS10. The root mean squared  
451 error (RMSE) for BACM of  $0.9 \text{ m s}^{-1}$  is improved to  $0.46 \text{ m s}^{-1}$  with the UACM. The under-  
452 prediction in T2 (MB and NMB) is greatly reduced by the UACM compared to BACM. Also, the  
453 T2 ME and NME decreased in the UACM by  $0.83 \text{ }^{\circ}\text{C}$  and 6% relative to the BACM. The  
454 metrics for RH2 other than IOA have shown a slight decrease in the performance by the UACM.  
455 A comparison of different statistical metrics for T2, RH2 and WS10 using the BACM and  
456 UACM models can be found in Table 2 while the definitions of the statistical metrics can be  
457 found in Appendix A.

458 Figures 6(a-c) show vertical profiles of the RH, potential temperature ( $\theta$ ), and WS at the  
459 Ayanagar station during the dense fog event on 30-Jan-2017 at 05:30 IST. These profiles offer  
460 valuable insights into the atmospheric stability conditions during the fog event. As depicted in  
461 Figure 6a, the RH profile illustrates that there is a complete air saturation (RH = 100%) within  
462 the depth of the fog layer. The UACM simulated a fog layer thickness of up to 60 meters, which  
463 was 30 meters lower than the BACM. The higher temperatures over the urban region due to the  
464 UHI effect, resulted in less condensation of liquid droplets in the UACM and a lower fog layer  
465 depth. It is worth noting that the observation profile exhibited an even smaller depth of fog layer.  
466 This difference could be due to the 1-km horizontal grid spacing of the model and a possible  
467 interpolation error while using the nearest model grid cell for comparison. Figure 6b presents the  
468 vertical profile for  $\theta$ . Both models show a well-mixed layer condition within the fog layer depth,  
469 indicating neutral stability. However, there is a slight instability near the ground due to the

warmer temperatures near the surface caused by the UHI effect, longwave warming inside the fog layer, and latent heat released during the liquid condensation process. In Figure 6c, the wind speed profiles demonstrate that the wind does not follow a logarithmic pattern within the urban canopy layer. Instead, the wind gradually decreases due to calm wind conditions and the influence of the urban environment within the fog layer depth. Above the fog layer, the wind profiles exhibit a logarithmic pattern, indicating a more stable atmospheric layer. Overall, the vertical profiles provide valuable information about the atmospheric stability conditions during the dense fog event and highlight the impact of the UHI effect on fog layer depth, the well-mixed layer condition within the fog layer, and the gradual decrease in wind speed within the urban canopy.

480

### 481 **3.2 Clear Sky Case (December 20-22, 2016)**

482 Figures 7(a-d) illustrate spatial T2 differences (UACM – BACM) at 06:00 IST, 09:00  
483 IST, 21:00 IST, and 03:00 IST on 20-Dec-2016 with clear skies and abundant sunshine (no-fog  
484 case). The UACM is considerably warmer than BACM at night (06:00 IST, 21:00 IST, and 03:00  
485 IST) but similar (09:00 IST, Figure 7b) or slightly cooler (14:00 IST, Figure S7b in the  
486 supporting information) during daytime. UACM reveals 8-18% RH2 reduction over urban areas  
487 compared to BACM (Figures 7(e-h)), which stems from nighttime urban warming, thereby urban  
488 air remaining away from the saturation point as discussed in the previous section. The spatial  
489 difference in wind speeds using BACM and UACM models presented in Figures 7(i-l) showed  
490 reduced wind speeds in UACM simulations, owing to appropriate consideration of momentum  
491 drag due to the presence of buildings (Figure S8 in the supporting information). In contrast, the  
492 surrounding regions of the urban areas exhibit slight increases in wind speeds. This could be due  
493 to the formation of rural-urban breezes, which are influenced by temperature variations and  
494 pressure gradients that drive the movement of air, between urban and rural areas, resulting in  
495 slightly windy conditions in the surrounding areas compared to the urban core.

496 Figures 8(a-c) depict the time-series plots of the bias between the modeled data and  
497 observations for T2, RH2, and WS10. Bold and dashed lines represent the bias of UACM and  
498 BACM, respectively. Positive values denote over-prediction; negative values signify under-  
499 prediction. Closer trends to zero-line suggest reduced differences. The UACM demonstrates  
500 significant enhancements in simulating daytime T2, as illustrated in Figure 8a. The model

501 successfully reduced the bias by creating a cooling effect during daytime, which mitigates the  
502 over-prediction of daytime temperatures exhibited by the BACM. The UACM has also reduced  
503 the daytime RH2 bias in Delhi, as depicted in Figure 8b. However, during nighttime, the UACM  
504 exhibits a dry bias compared to the BACM. This is due to the over-prediction of nighttime  
505 temperatures (warm bias) by the UACM possibly due to increased absorption of daytime sun  
506 rays and their multiple reflections within the canyons, which leads to the excessive evaporation  
507 and consequently lower moisture content. Nevertheless, certain stations such as Ayanagar,  
508 Jafarpur, and Akshardham demonstrate improvements in simulating nighttime temperatures. The  
509 UACM demonstrates improvements in simulating WS10 by accounting for the influence of  
510 urban structures and their effects on wind flow, as evident from the time-series plots at all the  
511 meteorological stations considered (Figure 8c). The statistical analysis presented in Table 2  
512 shows that the overall performance of UACM is better compared to BACM under clear sky  
513 conditions.

514 Figure 6 (d-f) presents the vertical profiles of RH, potential temperature ( $\theta$ ), and WS  
515 simulated by the UACM and BACM, along with the comparison to radiosonde observations at  
516 Ayanagar station. The RH profiles exhibit a dry bias (under-prediction) compared to the  
517 observation profile. This under-prediction is mainly attributed to the higher temperatures  
518 simulated by the UACM near the urban ground surface and within the urban canopy, as shown in  
519 Figure 6d. Note that the UACM RH profile is almost a mirror image of the  $\theta$  profile (Figure 6e).  
520 However, 90 meters AGL, the RH profiles for both models closely resemble each other. The  
521 potential temperature ( $\theta$ ) profiles demonstrate better agreement with the observation profile,  
522 particularly near the ground surface. The profiles exhibit a slightly convective nature at the  
523 Ayanagar station. Within the urban canopy, the UACM profiles show characteristics of a more  
524 well mixed layer up to a height of 50 m AGL, transitioning to a stable condition above it at 05:30  
525 IST, as depicted in Figure 6e. The WS profiles exhibit a logarithmic nature within the urban  
526 canopy at Ayanagar station. The wind magnitude near the ground surface is approximately 3.0 m  
527  $s^{-1}$  in the UACM, slightly deviating from the observed value. However, above the ground  
528 surface, some bias is still observed between the model profiles and the observation profile. This  
529 discrepancy may be attributed to the differences in distance between the nearby urban grid cell  
530 center and the exact location of the Ayanagar radiosonde observation site.

531

532     **4. Summary**

533     This study implemented the newly developed multilayer WRF-UACM by Dy et al.  
534     (2019) and Bhautmage et al. (2022) over the Delhi region for urban fog prediction application.  
535     The goal was to have an enhanced representation of the urban roughness sublayer and predict  
536     meteorological variables within the urban canopy layer using the WRF-UACM. We evaluated  
537     the model's capacity to forecast fog formation, by comparing with in-situ observations including  
538     those taken at the Indira Gandhi International Airport (IGIA) site in New Delhi during the  
539     Winter Fog Experiment (WiFEX; Ghude et al., 2017) field campaign. The implementation of  
540     WRF-UACM over the Delhi region showed noteworthy improvements in urban meteorology  
541     within the boundary layer, both during a clear-sky period and a foggy event. Predictions for  
542     parameters such as 10-meter wind speed (WS10), 2-meter temperature (T2), and 2-meter relative  
543     humidity (RH2) exhibited good agreement with observations from meteorological stations in  
544     Delhi. Notably, the UACM has contributed to the faster dissipation of fog compared to control  
545     (WRF-BACM) model runs, and this alignment with satellite images from NASA's MODIS  
546     sensor confirmed the clearing of fog over Delhi's urban region. In addition to the urban  
547     morphology, topography, and surface characteristics, the fog episodes are also influenced by  
548     numerous other factors such as synoptic scale weather patterns, regional moisture intrusion,  
549     aerosol loading, and microphysics related to the fog formation etc. The UACM model also  
550     demonstrated advancements in simulating fog timing, onset, and dissipation compared to  
551     visibility and liquid water content (LWC) observations at the IGIA site. Due to its computational  
552     efficiency, UACM is well-suited for operational fog forecasting. This has significant benefits for  
553     transportation and aviation sectors, reducing economic losses, health risks, and potential  
554     accidents due to low visibility. Overall, implementing UACM in operational mode, especially  
555     during winter, presents substantial advantages, as this study demonstrates. Moreover, assessing  
556     its performance in predicting various fog types like advection-radiation, cloud-base-lowering,  
557     evaporation, and precipitation fog would enhance the model's robustness. By offering improved  
558     accuracy in simulating urban meteorology and forecasting fog events, the model facilitates  
559     timely preventive actions and mitigates potential disruptions across sectors.

560  
561

562 **Acknowledgements**

563 We are thankful to Dr. Narendra Nigam from the Indian Meteorological Department (IMD),  
564 New Delhi, India for providing the essential meteorological stations data in the urbanized region  
565 of Delhi. Special thanks are also to the High-Performance Computing (HPC) Pratyush team at  
566 the Indian Institute of Tropical Meteorology (IITM), Pune, India for their continuous technical  
567 support in assisting with the WRF-UACM model setup and compiling issues. The authors also  
568 acknowledge GMR and Airport Authority of India for their logistic support at IGI Airport New  
569 Delhi. Finally, we would like to thank reviewers for their insightful and invaluable comments for  
570 improving the manuscript.

571

572 **Appendix A: Statistical Metrics Definitions**

573 In this study, the performance of the models is assessed using several statistical  
574 parameters, including the index of agreement (IOA), root mean square error (RMSE), mean bias  
575 (MB), normalized mean bias (NMB), mean error (ME), and normalized mean error (NME). The  
576 IOA measures the agreement between the model predictions and observations, with a value of 1  
577 indicating a perfect match and 0 indicating no agreement (Willmott, 1981). The RMSE and ME  
578 provide information about the average error in absolute magnitudes. The NME, expressed as a  
579 percentage, represents the average error relative to the observed values, where a higher NME  
580 indicates a greater error, and a lower value indicates a lesser error in the predictions. The MB  
581 indicates whether the model overestimates or underestimates compared to the observations. The  
582 NMB, also expressed as a percentage, indicates the average bias relative to the observed values,  
583 with a positive NMB indicating overestimation and a negative NMB indicating underestimation  
584 of the magnitudes.  $N$  is the total number of observations over a period at each individual  
585 meteorological station;  $M_i$  is the  $i$ th model simulated value corresponding to the  $i$ th observation  
586 value  $O_i$ ;  $\bar{O}$  is the average of observation values over a period.

587

588 
$$IOA = 1 - \frac{\sum_{i=1}^N (M_i - O_i)^2}{\sum_{i=1}^N (|M_i - \bar{O}| + |O_i - \bar{O}|)^2} \quad (\text{Eqn. A1})$$

589 
$$RMSE = \left[ \frac{1}{N} \sum_{i=1}^N (M_i - O_i)^2 \right]^{\frac{1}{2}} \quad (\text{Eqn. A2})$$

590

$$MB = \frac{\sum_{i=1}^N (M_i - O_i)}{N} \quad (\text{Eqn. A3})$$

591

$$NMB = \frac{\sum_{i=1}^N (M_i - O_i)}{\sum_{i=1}^N O_i} \quad (\text{Eqn. A4})$$

592

$$ME = \frac{\sum_{i=1}^N |M_i - O_i|}{N} \quad (\text{Eqn. A5})$$

593

$$NME = \frac{\sum_{i=1}^N |M_i - O_i|}{\sum_{i=1}^N O_i} \quad (\text{Eqn. A6})$$

594

595 **Disclaimer:**

596 Although this work was reviewed by the United States Environmental Protection Agency  
 597 (USEPA) and approved for publication, it may not necessarily reflect official Agency policy.  
 598 The mention of commercial products does not constitute endorsement by the Agency.

599

600 **Data Availability Statement**

601 Meteorological station observation data provided by the Indian Meteorological Department  
 602 (IMD, Delhi) <https://rmcnewdelhi.imd.gov.in> and Winter Fog Experiment (WiFEX 2017-18  
 603 Field Campaign) have been used to compare the models' performance in this manuscript. The  
 604 WiFEX field campaign data at Indira Gandhi International Airport (IGIA), New Delhi, India is  
 605 available from <https://ews.tropmet.res.in/wifex/observations.php> [Dataset].

606 The urban land-use data have been updated in the Delhi region from the European Space Agency  
 607 (ESA) World Cover 2021 data (released on October 28, 2022) based on Sentinel-1 and Sentinel-  
 608 2 satellite data which is available at <https://worldcover2021.esa.int> [Dataset].

609 The urban morphological parameters dataset required to run the WRF-UACM model were  
 610 developed by using the Geographic Information System (GIS) (ArcGIS V10.5.1) software,  
 611 which can be accessed at <https://www.esri.com/en-us/arcgis/products/arcgis-pro/overview>  
 612 [Software].

613 The Delhi region building shapefile along with the embedded building height data has been used  
614 to derive the urban morphological parameters which has been obtained from the UT-GLOBUS  
615 dataset (Kamath et al., 2022) [Dataset].

616 OpenStreetMap shapefile obtained from <https://www.geofabrik.de/data/download.html> has been  
617 used to develop street orientation parameter in the GIS (ArcGIS V10.5.1) software [Dataset].

618 The state-of-the-art Weather Research and Forecasting (WRF V3.8) model is available at  
619 <https://www2.mmm.ucar.edu> [Software]. The meteorological input data to create the initial and  
620 boundary conditions for the WRF model domains were obtained from the National Centers for  
621 Environmental Prediction (NCEP) FNL (Final) Operational Global Analysis data available at  
622 <https://rda.ucar.edu/datasets> [Dataset].

623 Figures have been made with the National Center for Atmospheric Research (NCAR) Command  
624 Language (NCL V6.3.0) post-processing tool accessible at <https://www.ncl.ucar.edu> [Software]  
625 and wrf-python plotting package available at <https://anaconda.org/conda-forge/wrf-python>  
626 [Software]. The radiometer liquid water content plot has been prepared with RPG-HATPRO  
627 Humidity and Temperature Profiler V8.79 [Software].

628 Radiosonde profiles at IMD, Ayanagar Station, New Delhi, India during study period are  
629 available from the Wyoming website: <https://weather.uwyo.edu/upperair/sounding.html>.  
630 LWC Plot was created using RAOB V6.8 [Software].

631  
632

## 633 **References**

- 634 AMS Glossary. (2020). *American Meteorological Society*.  
635 [https://glossary.ametsoc.org/wiki/Urban\\_heat\\_island](https://glossary.ametsoc.org/wiki/Urban_heat_island).
- 636 Bari, D., Bergot, T., & Tardif, R. (2023). Fog Decision Support Systems: A Review of the Current  
637 Perspectives. *Atmosphere*, 14(8), 1314. <https://doi.org/10.3390/atmos14081314>.
- 638 Bergot, T., and D. Guedalia ( 1994). Numerical forecasting of radiation fog. Part I: Numerical model and  
639 sensitivity tests. *Mon. Wea. Rev.*, 122 , 1218–1230. [https://doi.org/10.1175/1520-0493\(1994\)122<1218:NFORFP>2.0.CO;2](https://doi.org/10.1175/1520-0493(1994)122<1218:NFORFP>2.0.CO;2).
- 641 Bergot, T., Escobar, J., & Masson, V. (2015). Effect of small-scale surface heterogeneities and buildings  
642 on radiation fog: Large-eddy simulation study at Paris–Charles de Gaulle airport. *Quarterly Journal  
643 of the Royal Meteorological Society*, 141(686), 285–298. <https://doi.org/10.1002/qj.2358>
- 644 Bhautmage, U. P., Fung, J. C. H., Pleim, J., & Wong, M. M. F. (2022). Development and Evaluation of a  
645 New Urban Parameterization in the Weather Research and Forecasting (WRF) Model. *Journal of*

- 646      *Geophysical Research: Atmospheres*, 127(16), e2021JD036338.  
647      <https://doi.org/10.1029/2021JD036338>.
- 648      Bhowmik, S. R., Sud, A. M., & Singh, C. (2004). Forecasting fog over Delhi-An objective method.  
649      *Mausam*, 55(2), 313-322. <https://doi.org/10.54302/mausam.v55i2.1096>
- 650      Bhushan, B., Trivedi, H. K. N., Bhatia, R. C., Dube, R. K., Giri, R. K., & Negi, R. S. (2003). On the  
651      persistence of fog over northern parts of India. *Mausam*, 54(4), 851-860.
- 652      Bougeault, P., & Lacarrere, P. (1989). Parameterization of orography-induced turbulence in a mesobeta-  
653      scale model. *Monthly Weather Review*, 117(8), 1872–1890. [https://doi.org/10.1175/1520-0493\(1989\)117<1872:pooiti>2.0.co;2](https://doi.org/10.1175/1520-0493(1989)117<1872:pooiti>2.0.co;2)
- 655      Chen, F., & Dudhia, J. (2001). Coupling an advanced land surface–hydrology model with the Penn State-  
656      NCAR MM5 modeling system. Part I: Model implementation and sensitivity. *Monthly Weather  
657      Review*, 129(4), 569–585. [https://doi.org/10.1175/15200493\(2001\)129<0569:caalsh>2.0.co;2](https://doi.org/10.1175/15200493(2001)129<0569:caalsh>2.0.co;2)
- 658      Chen, F., Kusaka, H., Bornstein, R., Ching, J., Grimmond, C. S. B., Grossman-Clarke, S., et al. (2011).  
659      The integrated WRF/urban modelling system: Development, evaluation, and applications to urban  
660      environmental problems. *International Journal of Climatology*, 31(2), 273–288.  
661      <https://doi.org/10.1002/joc.2158>
- 662      Dhangar, N. G., Lal, D. M., Ghude, S. D., Kulkarni, R., Parde, A. N., Pithani, P., ... & Rajeevan, M.  
663      (2021). On the conditions for onset and development of fog over New Delhi: an observational study  
664      from the WiFEX. *Pure and Applied Geophysics*, 178, 3727-3746. <https://doi.org/10.1007/s00024-021-02800-4>
- 666      Dhangar, N. G., and Coauthors (2022). Fog nowcasting over the IGI Airport, New Delhi, India using  
667      decision tree. *Mausam*, 73, 785–794, <https://doi.org/10.54302/mausam.v73i4.3441>.
- 668      Dy, C. Y., Fung, J. C. H., & Pleim, J. (2019). Momentum drag effect over urbanized areas in the ACM2  
669      PBL component of the WRF model. *Journal of Geophysical Research: Atmospheres*, 124(8), 4460-  
670      4476. <https://doi.org/10.1029/2018JD029333>
- 671      Gao, X., Gao, S., & Yang, Y. (2018). A comparison between 3DVAR and EnKF for data assimilation  
672      effects on the Yellow Sea fog forecast. *Atmosphere*, 9(9), 346. <https://doi.org/10.3390/atmos9090346>
- 673      Gautam, R., Hsu, N. C., Kafatos, M., & Tsay, S. C. (2007). Influences of winter haze on fog/low cloud  
674      over the Indo-Gangetic plains. *Journal of Geophysical Research: Atmospheres*, 112(D5).  
675      <https://doi.org/10.1029/2005JD007036>
- 676      Gautam, R., & Singh, M. K. (2018). Urban heat island over Delhi punches holes in widespread fog in the  
677      Indo-Gangetic Plains. *Geophysical Research Letters*, 45(2), 1114-1121.  
678      <https://doi.org/10.1002/2017GL076794>
- 679      Geofabrik Download Server. (2018). OpenStreetMap Data Extracts [WWW Document]. Retrieved from  
680      <https://www.geofabrik.de/data/download.html>

- 681 Ghude, S. D., Bhat, G. S., Prabhakaran, T., Jenamani, R. K., Chate, D. M., Safai, P. D., ... & Rajeevan,  
682 M. (2017). Winter fog experiment over the Indo-Gangetic plains of India. *Current Science*, 767-784.  
683 DOI:10.18520/cs/v112/i04/767-784.
- 684 Ghude, S. D., Jenamani, R. K., Kulkarni, R., Wagh, S., Dhangar, N. G., Parde, A. N., ... & Rajeevan, M.  
685 (2023). WiFEX: Walk into the Warm Fog over Indo-Gangetic Plain Region. *Bulletin of the American  
686 Meteorological Society*, 104(5), E980-E1005. <https://doi.org/10.1175/BAMS-D-21-0197.1>
- 687 Gu, Y., Kusaka, H., & Tan, J. (2019). Impacts of urban expansion on fog types in Shanghai, China:  
688 Numerical experiments by WRF model. *Atmospheric Research*, 220, 57-74.  
689 <https://doi.org/10.1016/j.atmosres.2018.12.026>
- 690 Gunturu, U. B., & Kumar, V. (2021). Weakened Baroclinic Activity Causes an Abrupt Rise in Fog in the  
691 Indo-Gangetic Plain. *Geophysical Research Letters*, 48(24), e2021GL096114.  
692 <https://doi.org/10.1029/2021GL096114>
- 693 Hendricks, E. A., Knievel, J. C., & Wang, Y. (2020). Addition of multilayer urban canopy models to a  
694 nonlocal planetary boundary layer parameterization and evaluation using ideal and real cases. *Journal  
695 of Applied Meteorology and Climatology*, 59(8), 1369-1392.
- 696 Hingmire, D., Vellore, R. K., Krishnan, R., Ashtikar, N. V., Singh, B. B., Sabade, S., & Madhura, R. K.  
697 (2019). Widespread fog over the Indo-Gangetic Plains and possible links to boreal winter  
698 teleconnections. *Climate Dynamics*, 52, 5477-5506. <https://doi.org/10.1007/s00382-018-4458-y>
- 699 Hingmire, D., Vellore, R., Krishnan, R., Singh, M., Metya, A., Gokul, T., & Ayantika, D. C. (2021).  
700 Climate change response in wintertime widespread fog conditions over the Indo-Gangetic Plains.  
701 *Climate Dynamics*, 1-22. <https://doi.org/10.1007/s00382-021-06030-1>
- 702 Hong, S. Y., Noh, Y., & Dudhia, J. (2006). A new vertical diffusion package with an explicit treatment of  
703 entrainment processes. *Monthly Weather Review*, 134, 2318–2341.  
704 <https://doi.org/10.1175/MWR3199.1>
- 705 Janjić, Z. I. (1994). The step-mountain eta coordinate model: Further developments of the convection,  
706 viscous sublayer, and turbulence closure schemes. *Monthly Weather Review*, 122(5), 927–945.  
707 [https://doi.org/10.1175/1520-0493\(1994\)122<0927:TSMECM>2.0.CO;2](https://doi.org/10.1175/1520-0493(1994)122<0927:TSMECM>2.0.CO;2)
- 708 Jayakumar, A., Rajagopal, E. N., Boutle, I. A., George, J. P., Mohandas, S., Webster, S., & Aditi, S.  
709 (2018). An operational fog prediction system for Delhi using the 330 m Unified Model. *Atmospheric  
710 Science Letters*, 19(1), e796. <https://doi.org/10.1002/asl.796>
- 711 Jayakumar, A., Gordon, H., Francis, T., Hill, A. A., Mohandas, S., Sandeepan, B. S., ... & Beig, G.  
712 (2021). Delhi Model with Chemistry and aerosol framework (DM-Chem) for high-resolution fog  
713 forecasting. *Quarterly Journal of the Royal Meteorological Society*, 147(741), 3957-3978.  
714 <https://doi.org/10.1002/qj.4163>
- 715 Jenamani, R. K. (2007). Alarming rise in fog and pollution causing a fall in maximum temperature over  
716 Delhi. *Current Science*, 314-322. <https://www.jstor.org/stable/24099461>

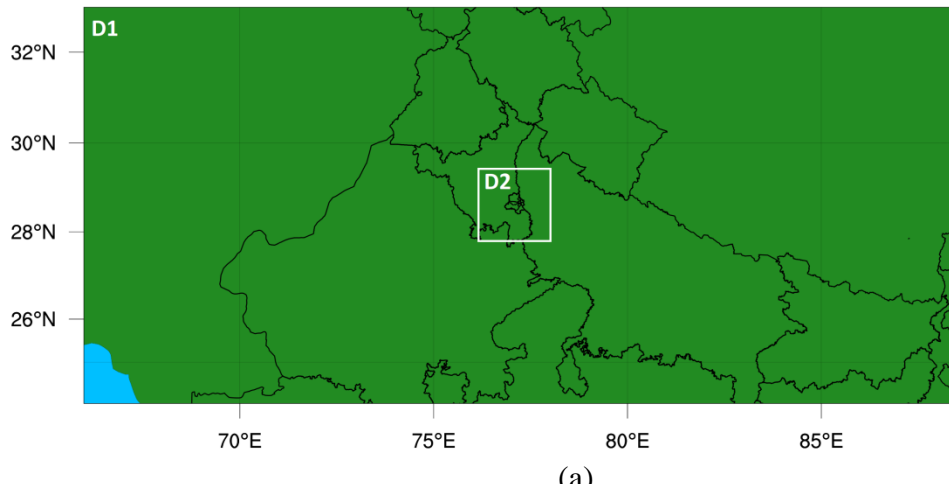
- 717 Kamath, H. G., Singh, M., Magruder, L. A., Yang, Z. L., & Niyogi, D. (2022). GLOBUS: GLObal  
718 Building heights for Urban Studies. *arXiv preprint arXiv:2205.12224*
- 719 Kusaka, H., Kondo, H., Kikegawa, Y., & Kimura, F. (2001). A simple single-layer urban canopy model  
720 for atmospheric models: Comparison with multi-layer and slab models. *Boundary-Layer  
721 Meteorology*, 101, 329–358. <https://doi.org/10.1023/a:1019207923078>
- 722 Müller, M. D., Schmutz, C., & Parlow, E. (2007). A one-dimensional ensemble forecast and assimilation  
723 system for fog prediction. *Pure and Applied Geophysics*, 164, 1241-1264.  
724 <https://doi.org/10.1007/s00024-007-0217-4>
- 725 Martilli, A., Clappier, A., & Rotach, M. W. (2002). An urban surface exchange parameterisation for  
726 mesoscale models. *Boundary-Layer Meteorology*, 104, 261–304.  
727 <https://doi.org/10.1023/a:1016099921195>
- 728 Masson, V. (2000). A physically-based scheme for the urban energy budget in atmospheric models.  
729 *Boundary-Layer Meteorology*, 94, 357–397. <https://doi.org/10.1023/a:1002463829265>
- 730 Mellor, G. L., & Yamada, T. (1974). A hierarchy of turbulence closure models for planetary boundary  
731 layers. *Journal of the Atmospheric Sciences*, 31(7), 1791–1806. [https://doi.org/10.1175/1520-0469\(1974\)031<1791:ahotcm>2.0.co;2](https://doi.org/10.1175/1520-0469(1974)031<1791:ahotcm>2.0.co;2)
- 733 Mellor, G. L., & Yamada, T. (1982). Development of a turbulence closure model for geophysical fluid  
734 problems. *Reviews of Geophysics*, 20(4), 851–875. <https://doi.org/10.1029/RG020i004p00851>
- 735 Niu, G. Y., Yang, Z. L., Mitchell, K. E., Chen, F., Ek, M. B., Barlage, M., ... & Xia, Y. (2011). The  
736 community Noah land surface model with multiparameterization options (Noah-MP): 1. Model  
737 description and evaluation with local-scale measurements. *Journal of Geophysical Research: Atmospheres*, 116(D12).
- 739 Pahlavan, R., Moradi, M., Tajbakhsh, S., Azadi, M., & Rahnama, M. (2021). Fog probabilistic forecasting  
740 using an ensemble prediction system at six airports in Iran for 10 fog events. *Meteorological  
741 applications*, 28(6), e2033. <https://doi.org/10.1002/met.2033>
- 742 Parde, A.N., Ghude, S.D., Dhangar, N.G., Lonkar, P., Wagh, S., Govardhan, G., Biswas, M. and  
743 Jenamani, R.K. (2022a). Operational probabilistic fog prediction based on Ensemble Forecast  
744 System: A decision support system for fog. *Atmosphere*, 13(10), 1608.  
745 <https://doi.org/10.3390/atmos13101608>.
- 746 Parde, A. N., Ghude, S. D., Sharma, A., Dhangar, N. G., Govardhan, G., Wagh, S., ... & Niyogi, D.  
747 (2022b). Improving simulation of the fog life cycle with high-resolution land data assimilation: A  
748 case study from WiFEX. *Atmospheric Research*, 278, 106331.  
749 <https://doi.org/10.1016/j.atmosres.2022.106331>
- 750 Parde, A.N., Ghude S.D., Dhangar, N.G., Bhautmage, U.P., Wagh, S., Lonkar, P., Govardhan, G., Kumar,  
751 R., Biswas, M., Chen, F. (2023). Challenges in Simulating Prevailing Fog Types over Urban Region  
752 of Delhi, *under-review*.

- 753 Pithani, P., Ghude, S. D., Jenamani, R. K., Biswas, M., Naidu, C. V., Debnath, S., ... & Rajeevan, M.  
754 (2020). Real-time forecast of dense fog events over Delhi: The performance of the wrf model during  
755 the wifex field campaign. *Weather and Forecasting*, 35(2), 739-756. <https://doi.org/10.1175/WAF-D-19-0104.1>
- 756
- 757 Price, J. D., A. Porson, and A. Lock (2015). An observational case study of persistent fog and comparison  
758 with an ensemble forecast model. *Bound.-Layer Meteor.*, 155, 301–327,  
759 <https://doi.org/10.1007/s10546-014-9995-2>.
- 760
- 761 Rémy, S., & Bergot, T. (2010). Ensemble Kalman filter data assimilation in a 1D numerical model used  
762 for fog forecasting. *Monthly weather review*, 138(5), 1792-1810.  
763 <https://doi.org/10.1175/2009MWR3110.1>
- 764 Sachweh, M., & Koepke, P. (1997). Fog dynamics in an urbanized area. *Theoretical and Applied  
765 Climatology*, 58, 87-93. <https://doi.org/10.1007/BF00867435>
- 766 Salamanca, F., & Martilli, A. (2010). A new building energy model coupled with an urban canopy  
767 parameterization for urban climate simulations—Part II. Validation with one dimension off-line  
768 simulations. *Theoretical and Applied Climatology*, 99, 345–356. <https://doi.org/10.1007/s00704-009-0143-8>
- 769
- 770 Sawaisarje, G. K., Khare, P., Shirke, C. Y., Deepakumar, S., & Narkhede, N. M. (2014). Study of winter  
771 fog over Indian subcontinent: Climatological perspectives. *Mausam*, 65(1), 19-28.  
772 <https://doi.org/10.54302/mausam.v65i1.858>
- 773 Singh, M.K., Gautam, R. (2022). Developing a long-term high-resolution winter fog climatology over  
774 south Asia using satellite observations from 2002 to 2020. *Remote Sens. Environ.* 279.  
775 <https://doi.org/10.1016/j.rse.2022.113128>
- 776 Singh, J. and Kant, S. (2006). Radiation fog over north India during winter from 1989-2004. *Mausam*,  
777 57(2), 271-290. <https://doi.org/10.54302/mausam.v57i2.474>
- 778 Singh, J., Giri, R. K., & Kant, S. (2007). Radiation fog viewed by INSAT-1 D and Kalpana Geo-  
779 Stationary satellite. *Mausam*, 58(2), 251-260.
- 780 Skamarock, W. C., Klemp, J. B., Dudhia, J., Gill, D. O., Barker, D. M., Duda, M. G., ... & Powers, J. G.  
781 (2008). A description of the advanced research WRF Version 3, Mesoscale and Microscale  
782 Meteorology Division. *National Center for Atmospheric Research, Boulder, Colorado, USA*, 88, 7-  
783 25.
- 784 Steeneveld, G.J., Ronda, R.J., Holtslag, A.A.M. (2015). The Challenge of Forecasting the Onset and  
785 Development of Radiation Fog Using Mesoscale Atmospheric Models. *Boundary-Layer Meteorol.*  
786 154. <https://doi.org/10.1007/s10546-014-9973-8>
- 787 Theethai Jacob, A., Jayakumar, A., Gupta, K., Mohandas, S., Hendry, M. A., Smith, D. K., ... & Ghude,  
788 S. (2023). Implementation of the urban parameterization scheme in the Delhi model with an  
789 improved urban morphology. *Quarterly Journal of the Royal Meteorological Society*, 149(750), 40-  
790 60. <https://doi.org/10.1002/qj.4382>

- 791 Van De Kerchove, R., Zanaga, D., Keersmaecker, W., Souverijns, N., Wevers, J., Brockmann, C., ... &  
 792 Arino, O. (2021). ESA WorldCover: Global land cover mapping at 10 m resolution for 2020 based on  
 793 Sentinel-1 and 2 data. In *AGU Fall Meeting Abstracts* (Vol. 2021, pp. GC45I-0915).  
 794 <https://worldcover2021.esa.int/>
- 795 Wagh, S., Kulkarni, R., Lonkar, P. *et al.* (2023). Development of visibility equation based on fog  
 796 microphysical observations and its verification using the WRF model. *Model. Earth Syst. Environ.* 9,  
 797 195–211. <https://doi.org/10.1007/s40808-022-01492-6>
- 798 Willmott, C. J. (1981). On the validation of models. *Physical geography*, 2(2), 184-194.  
 799 <https://doi.org/10.1080/02723646.1981.10642213>
- 800 Yadav, P., Parde, A.N., Dhangar, N.G., Govardhan, G., Lal, D.M., Wagh, S., Prasad, D.S.V.V.D.,  
 801 Ahmed,  
 802 R., Ghude, S.D. (2022). Understanding the genesis of a dense fog event over Delhi using  
 803 observations and high-resolution model experiments. *Model. Earth Syst. Environ.* 8.  
 804 <https://doi.org/10.1007/s40808-022-01463-x>
- 805 Zhou, B., & Du, J. (2010). Fog prediction from a multimodel mesoscale ensemble prediction system.  
 806 *Weather and Forecasting*, 25(1), 303-322. <https://doi.org/10.1175/2009WAF2222289.1>
- 808

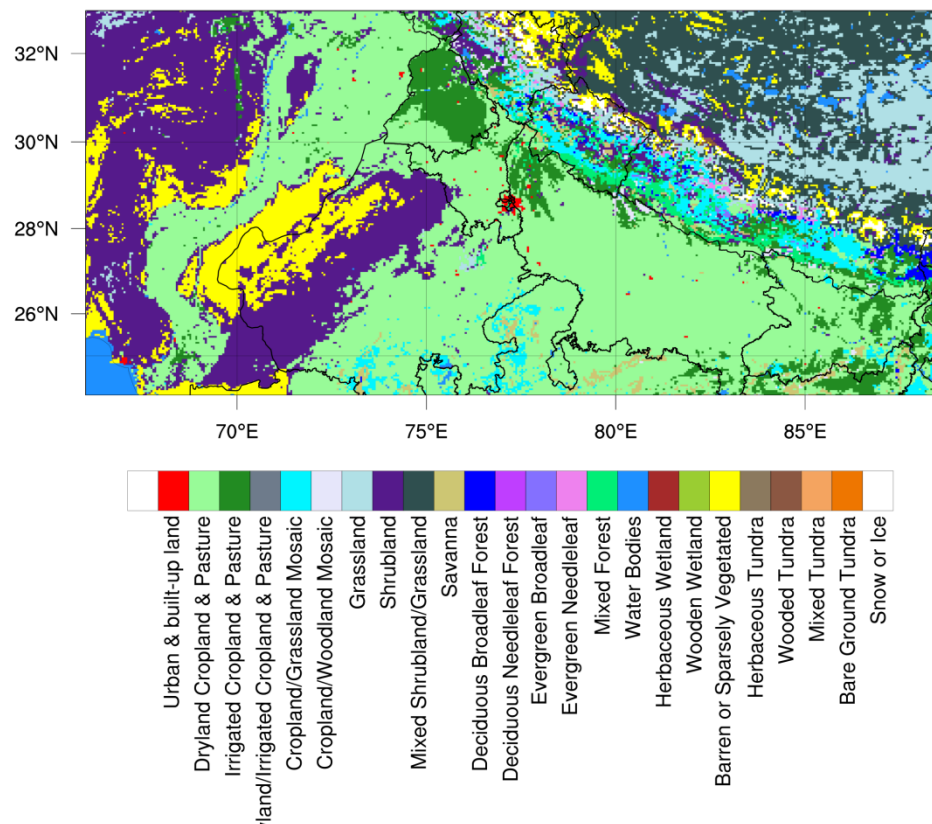
809 **Figures**

### WRF-Model Two Nested-Domains Configuration



810  
 811  
 812

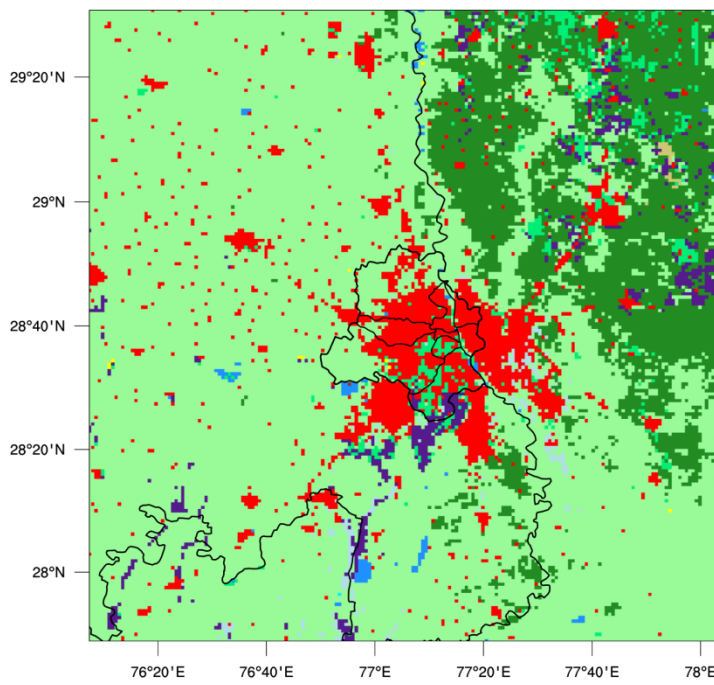
Landuse [IGP WRF USGS-Sentinel Domain-1]



813  
814

(b)

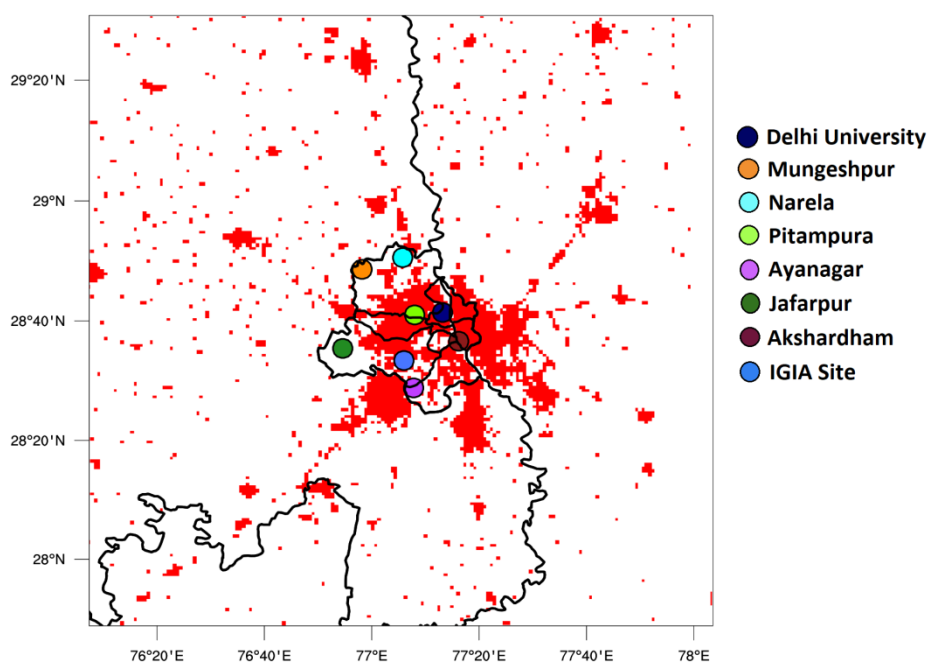
Landuse [IGP WRF USGS-Sentinel Domain-2]



(c)

815  
816  
817

[Urban Cells & Met. Station Locations]



(d)

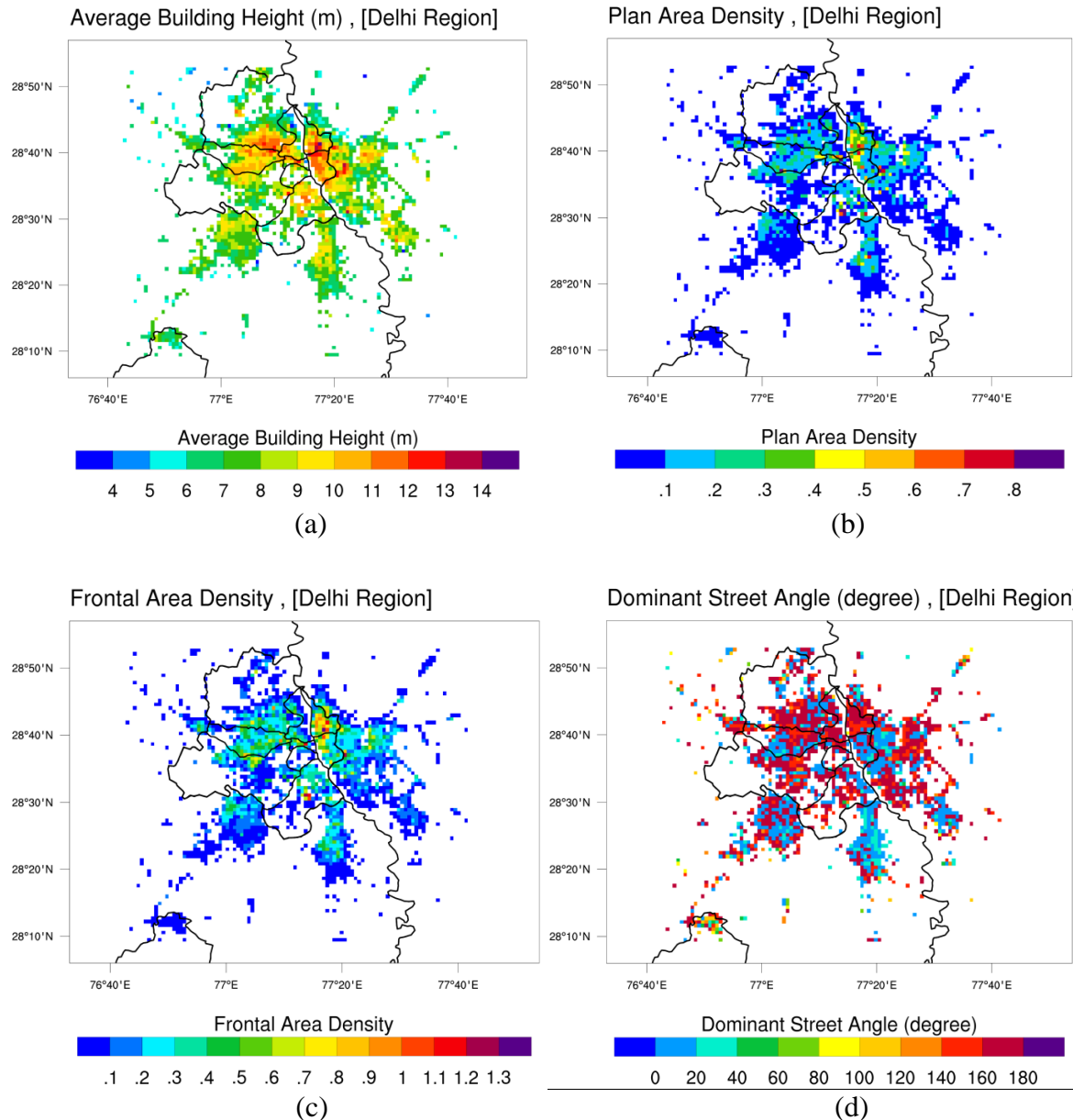
818  
819  
820

821 **Figure 1.** (a) Two nested domains setup over the Indo Gangetic Plain (IGP) region in Weather  
822 Research and Forecasting (WRF) model, (b-c) Updated USGS-Sentinel land-use and land-cover

823 (LULC) in Domain-1 (D1, 5-km grid spacing) and Domain-2 (D2, 1-km grid spacing), (d) Indian  
 824 Meteorological Department (IMD) station locations (circular symbols) in Delhi urban region for  
 825 verifying the model.

826

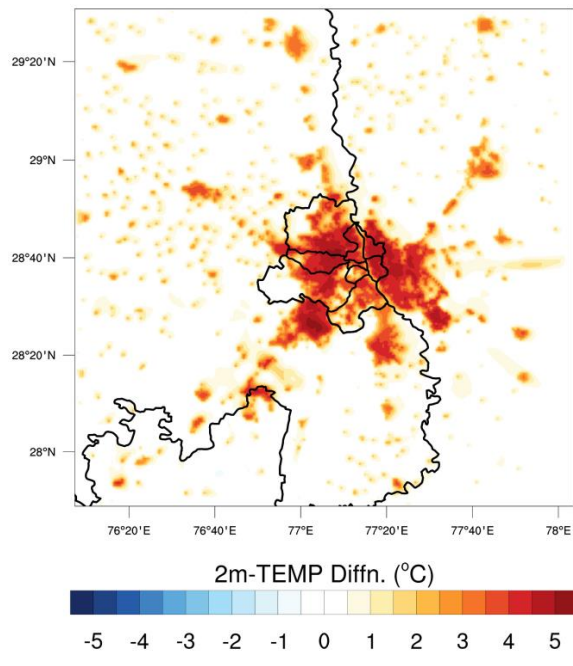
827



831  
 832  
 833  
 834 **Figure 2.** Delhi region urban morphological parameters dataset for (a) average building height  
 835 [ $H$ ], (b) plan area density [ $\lambda_p$ ], (c) frontal area density [ $\lambda_f$ ], and (d) street canyon orientation [ $\varphi$ ].

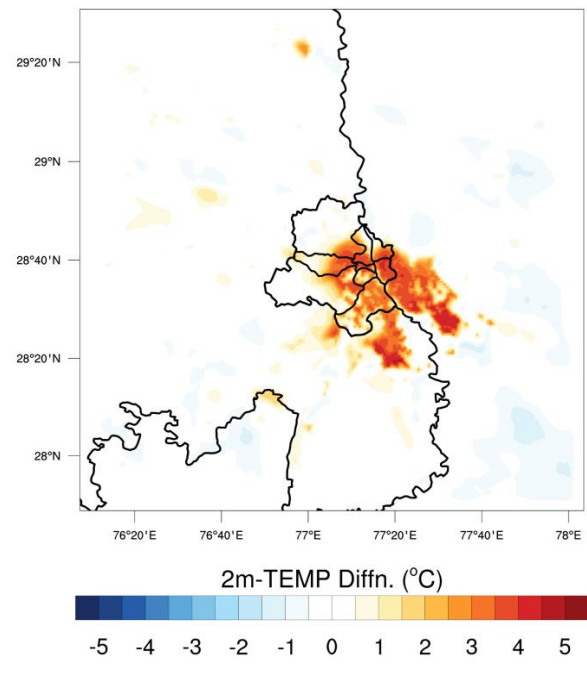
836

2m-TEMP Diffn. ( $^{\circ}$ C) [21:00 IST]



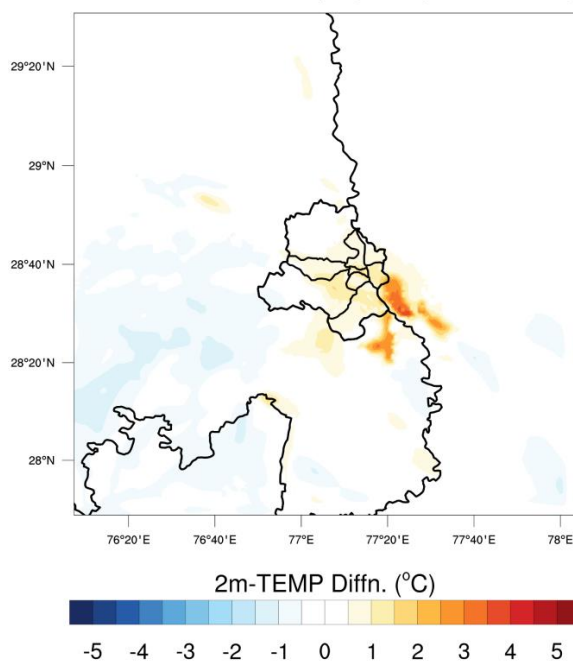
(a)

2m-TEMP Diffn. ( $^{\circ}$ C) [03:00 IST]



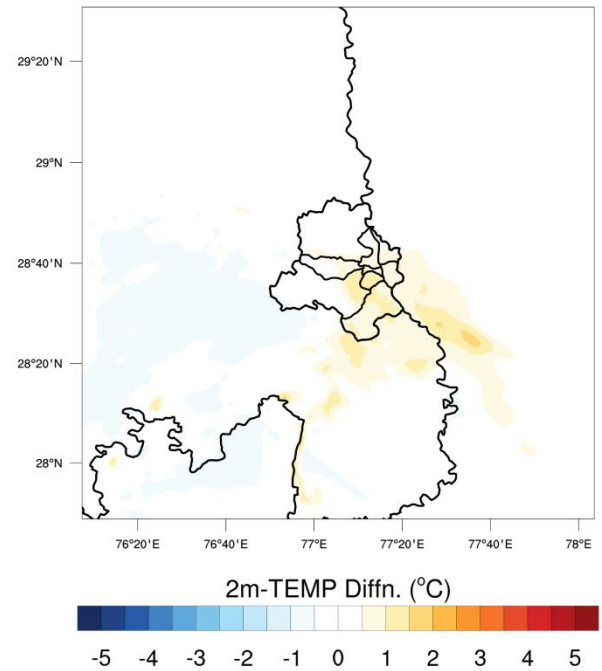
(b)

2m-TEMP Diffn. ( $^{\circ}$ C) [06:00 IST]



(c)

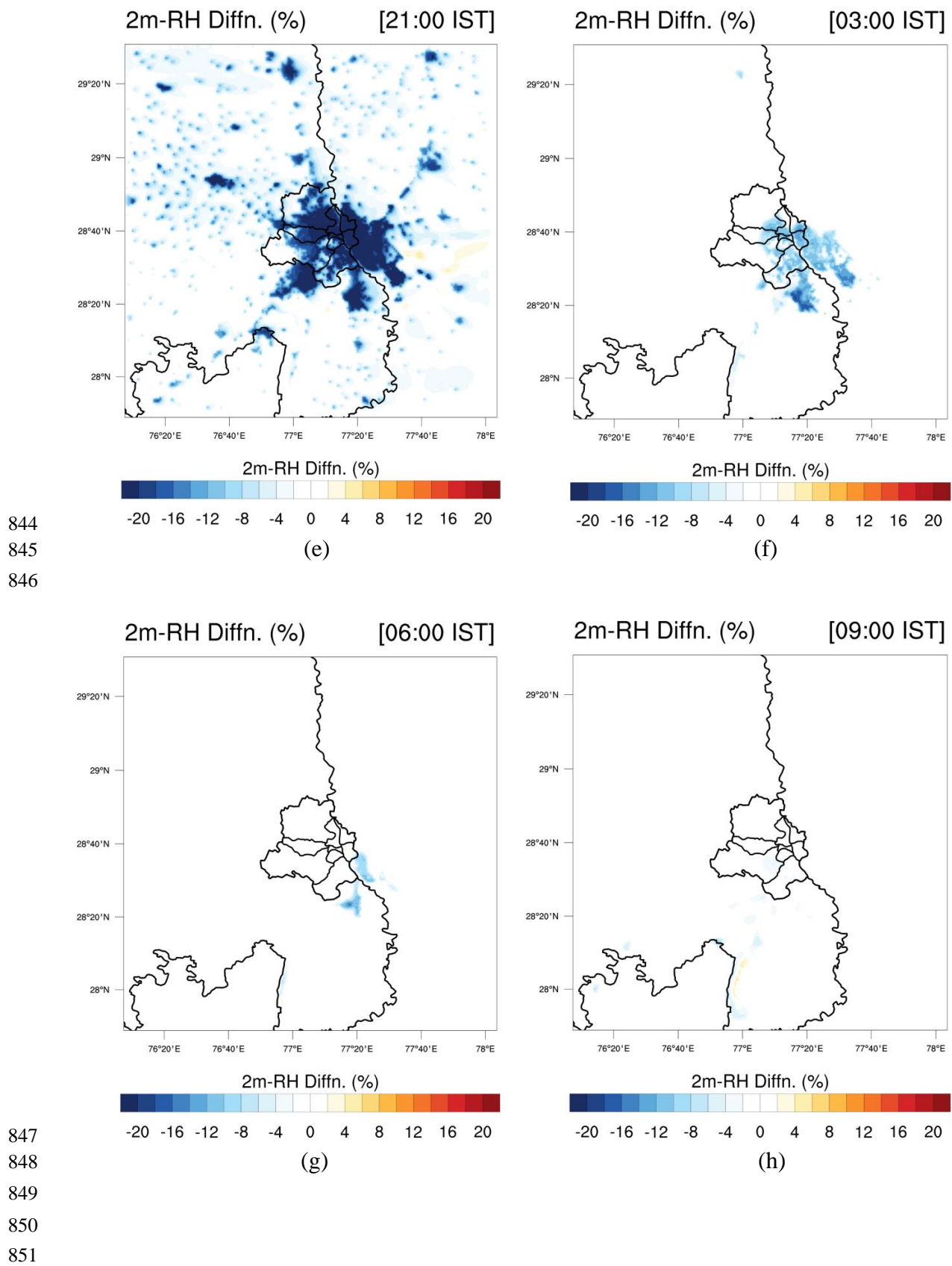
2m-TEMP Diffn. ( $^{\circ}$ C) [09:00 IST]

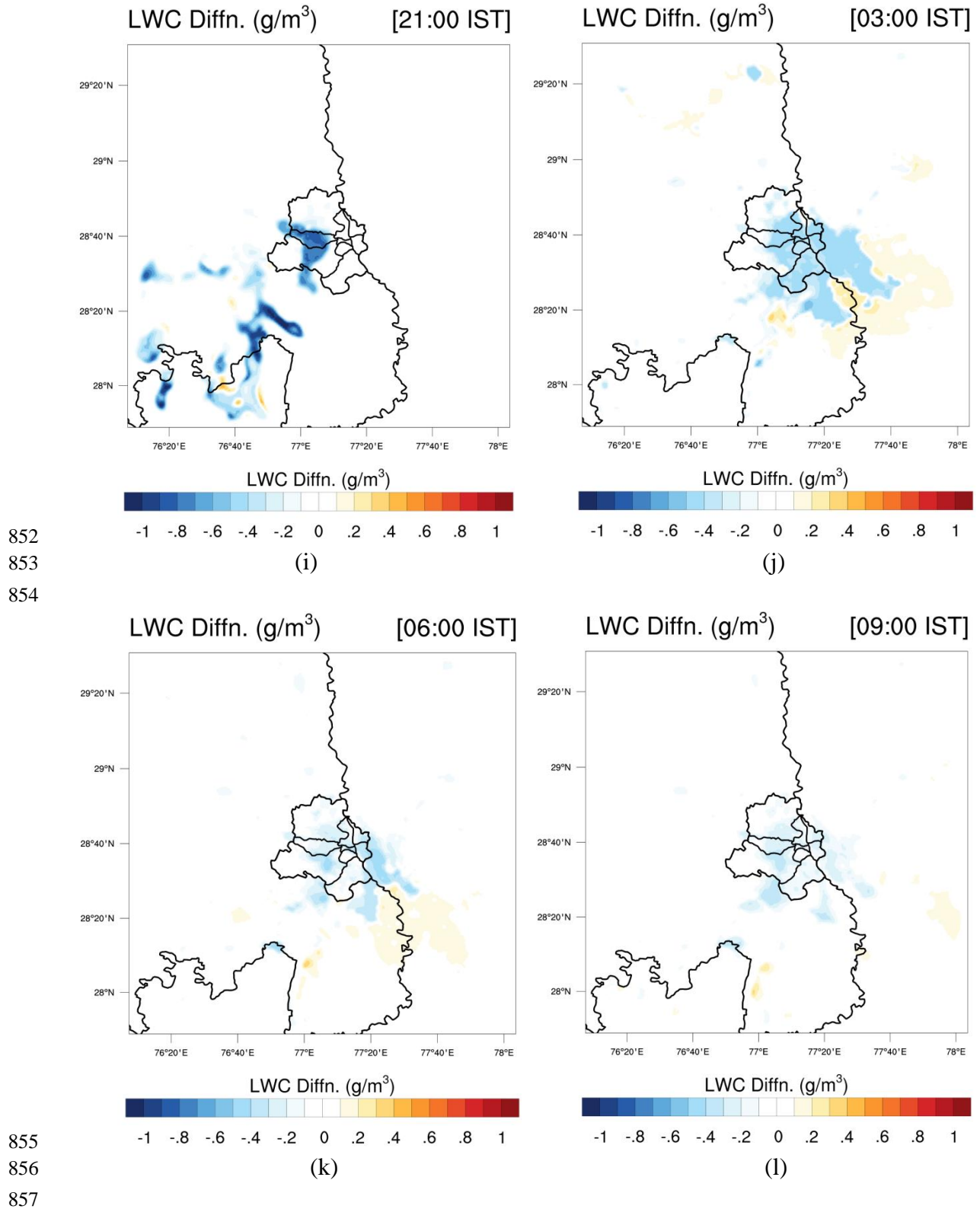


(d)

837  
838  
839

840  
841  
842  
843





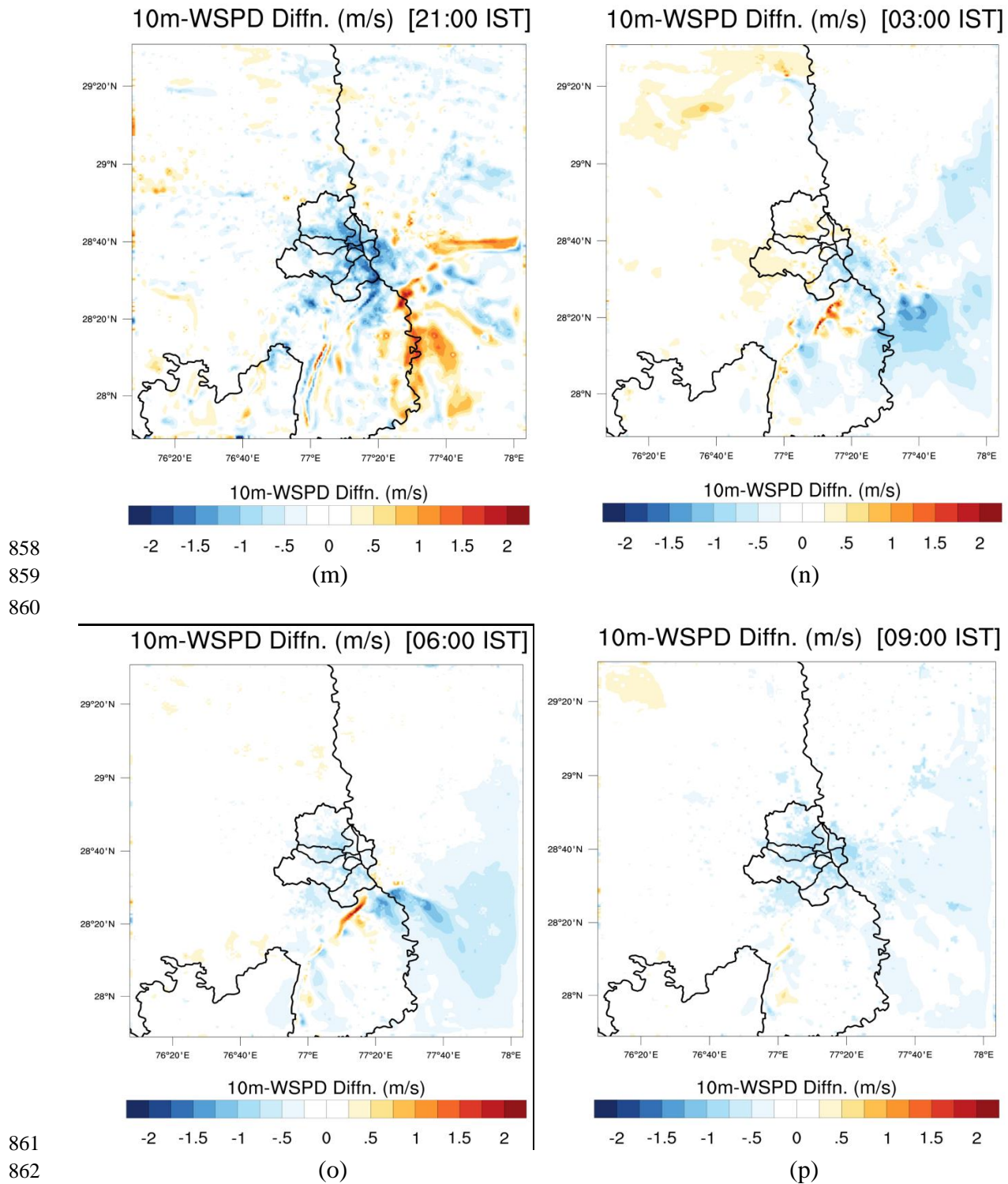


**Figure 3.** Contour plots of model difference [UACM – BACM] for (a-d) 2-m temperature, (e-h) 2-m relative humidity, (i-l) liquid water content at surface , and (m-p) 10-m wind speed during a fog event at 21:00 IST on 29 January 2017, and at 03:00 IST, 06:00 IST, 09:00 IST on 30 January 2017.

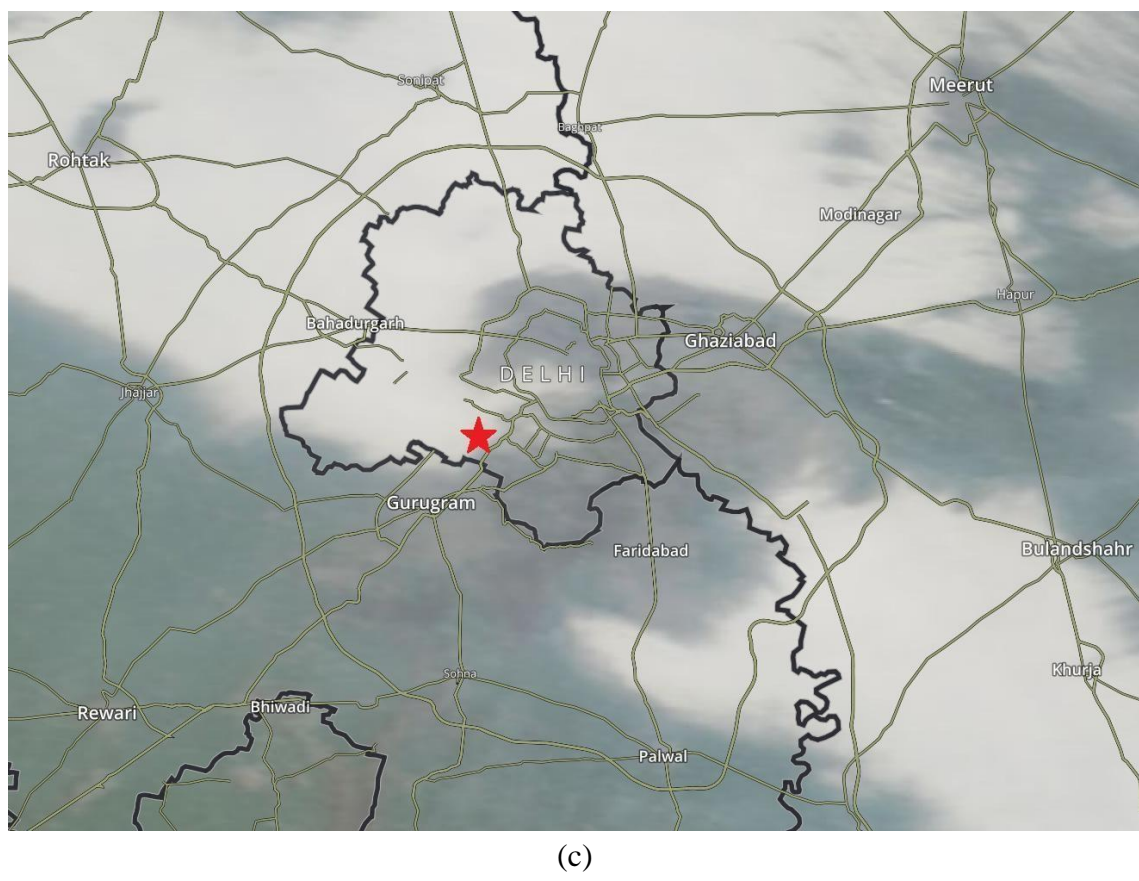
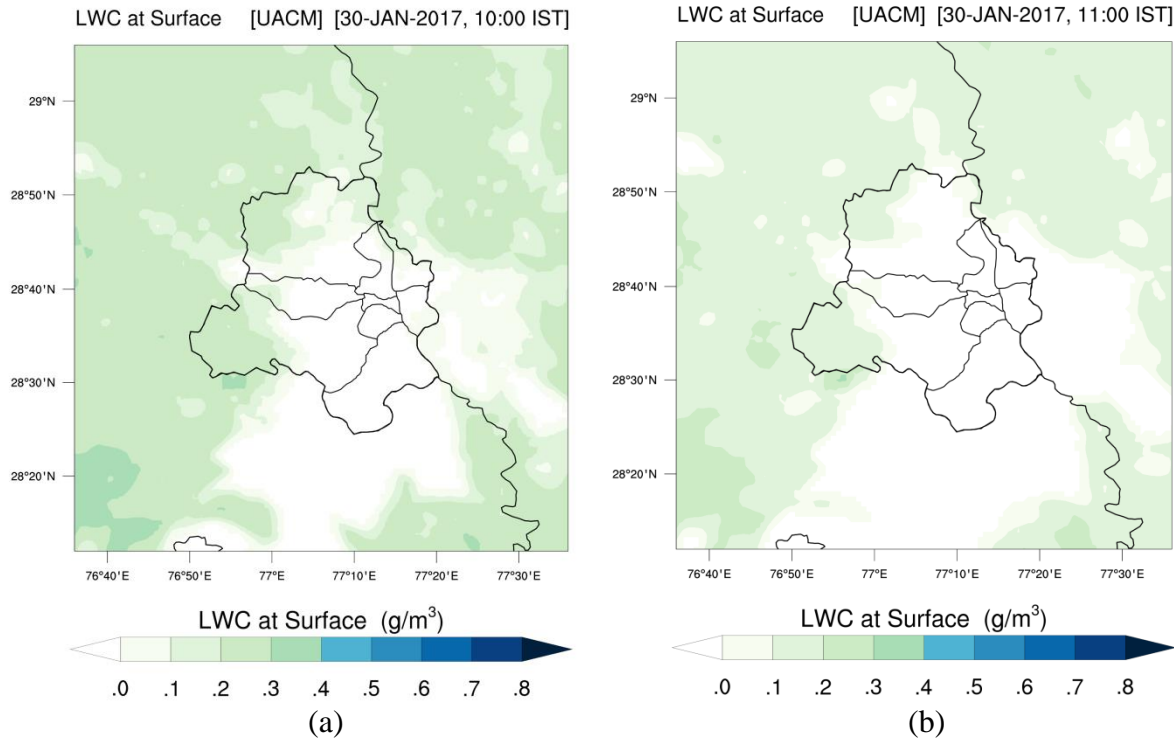
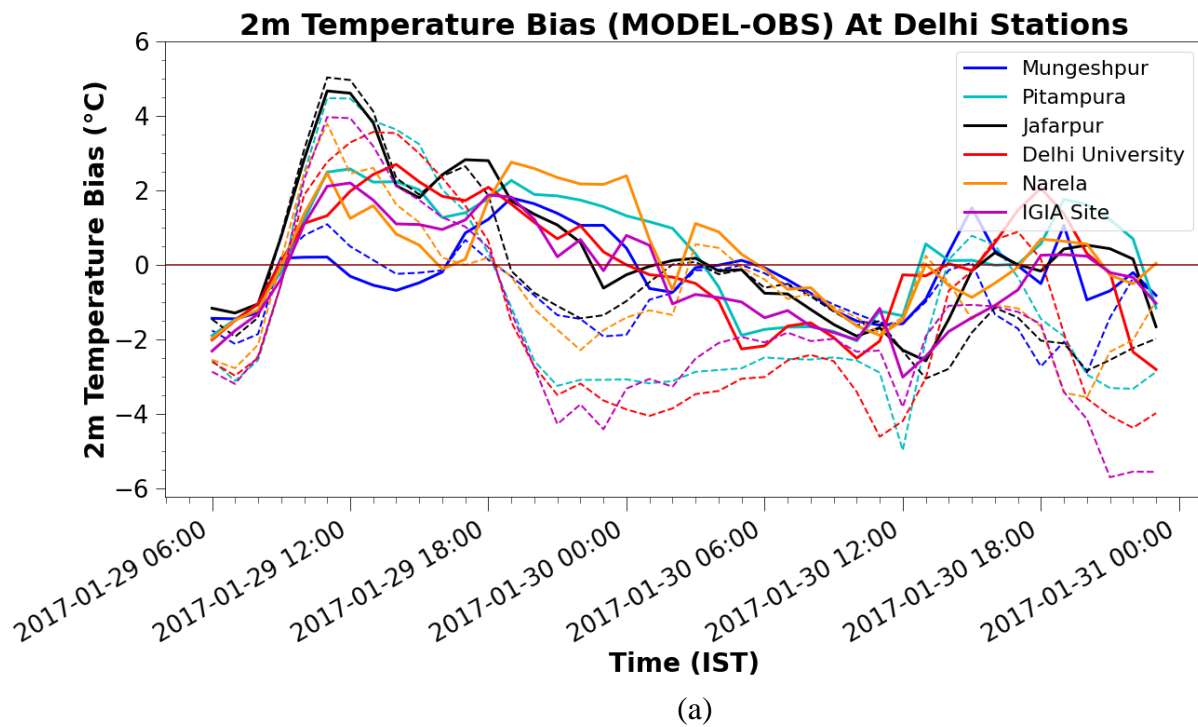


**Figure 4.** Contour plots of UACM liquid water content (LWC) at surface at (a) 10:00 IST, (b) 11:00 IST, and (c) a low cloud satellite image from NASA's MODIS (Moderate Resolution

874 Imaging Spectroradiometer) captured at approximately 10:30 am IST on January 30, 2017,  
875 during a fog event over the Delhi region. The 'red star' symbol marks the location of the Delhi  
876 Indira Gandhi International Airport (IGIA) at 28.5562° N, 77.100° E.

877

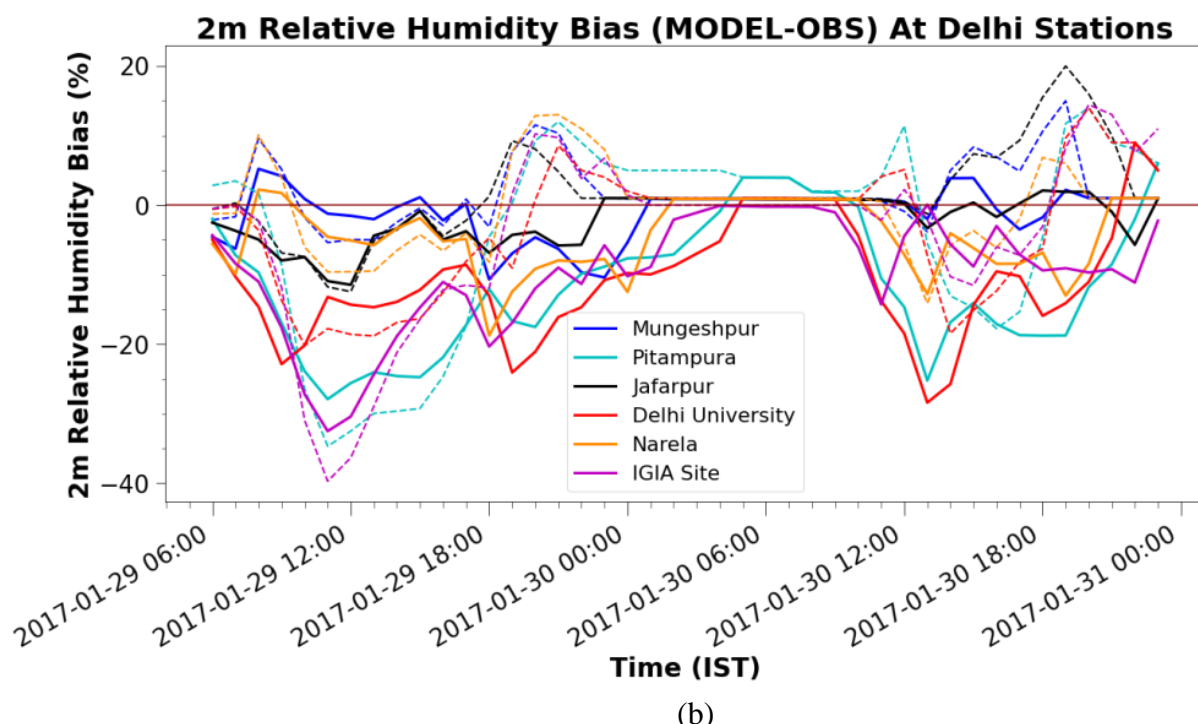
878



879

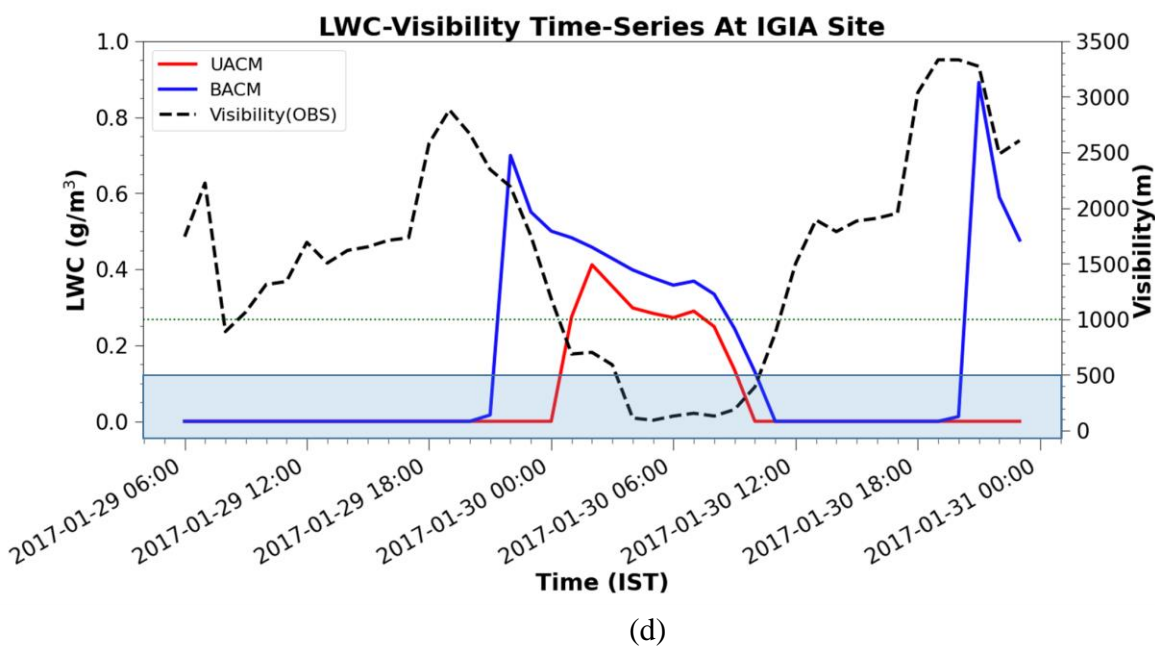
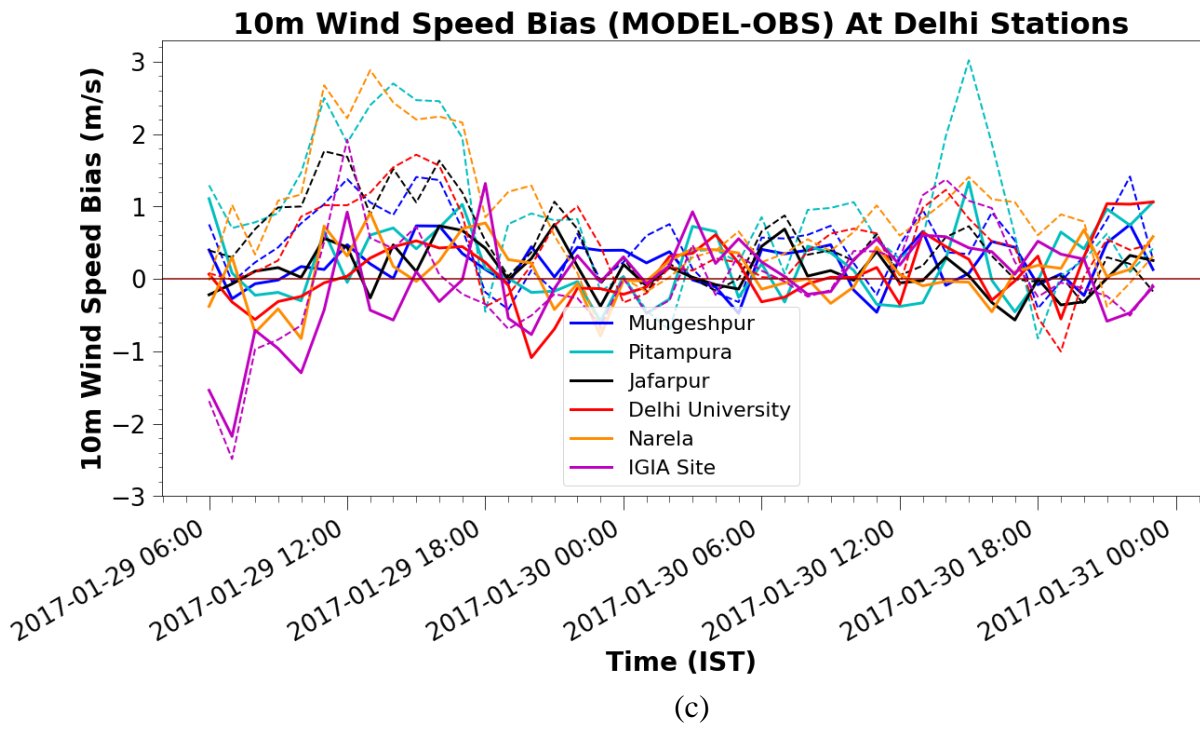
880

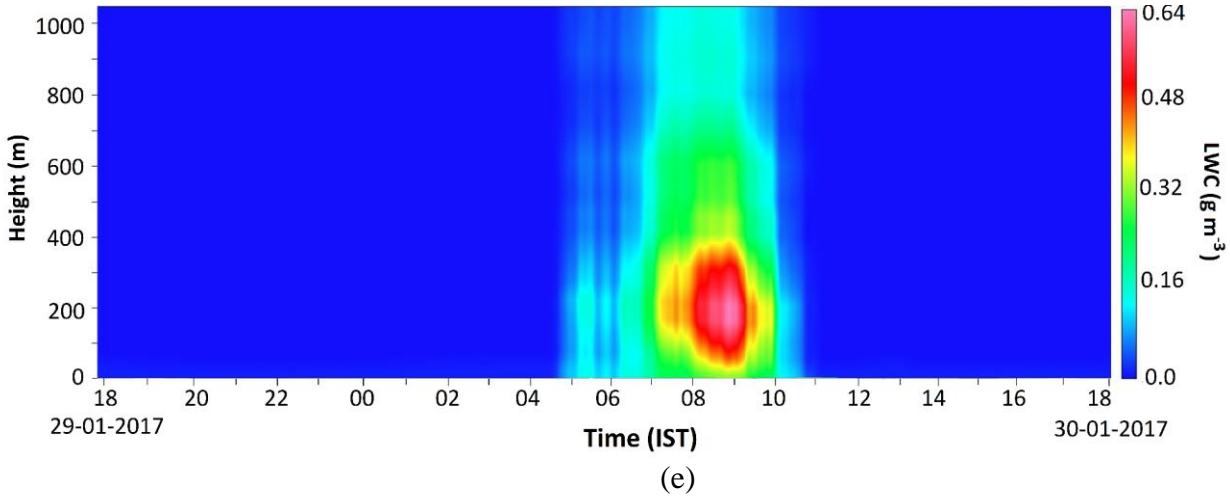
881



882

883

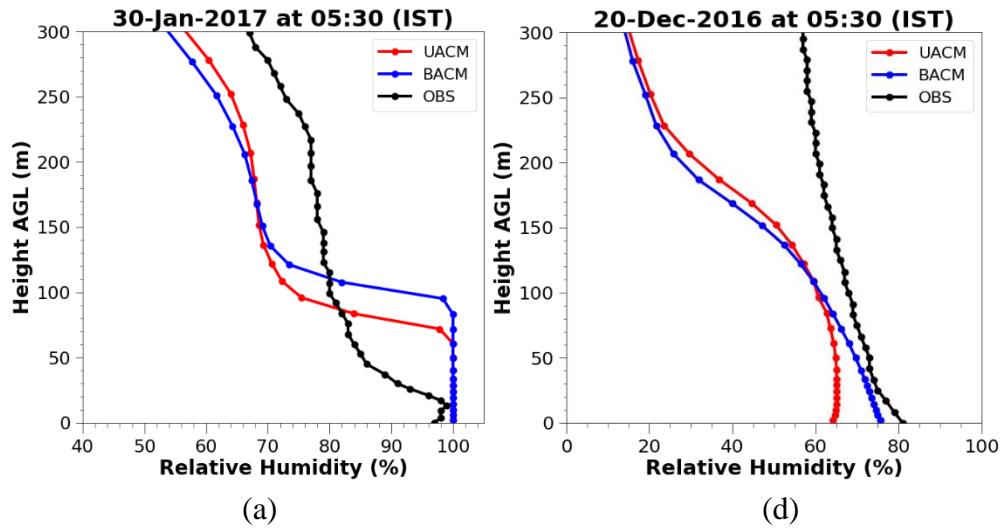




(e)

**Figure 5.** Time-series bias plots [MODEL – OBS] (bold line: UACM, dashed line: BACM) for (a) 2-m temperature, (b) 2-m relative humidity, (c) 10-m wind speed at Delhi urban Indian Meteorological Department (IMD) stations, (d) time-series comparison of models liquid water content (LWC) at the surface with visibility data at the Indira Gandhi International Airport (IGIA) site from 29-Jan-2017 (06:00 IST) to 30-Jan-2017 (23:00 IST), and (e) radiometer LWC observations at the IGIA site during a fog event case. UACM: Urban Asymmetric Convective Model; BACM: Base Asymmetric Convective Model (WRF model control runs); OBS: Observations.

899



(a)

(d)

900  
901

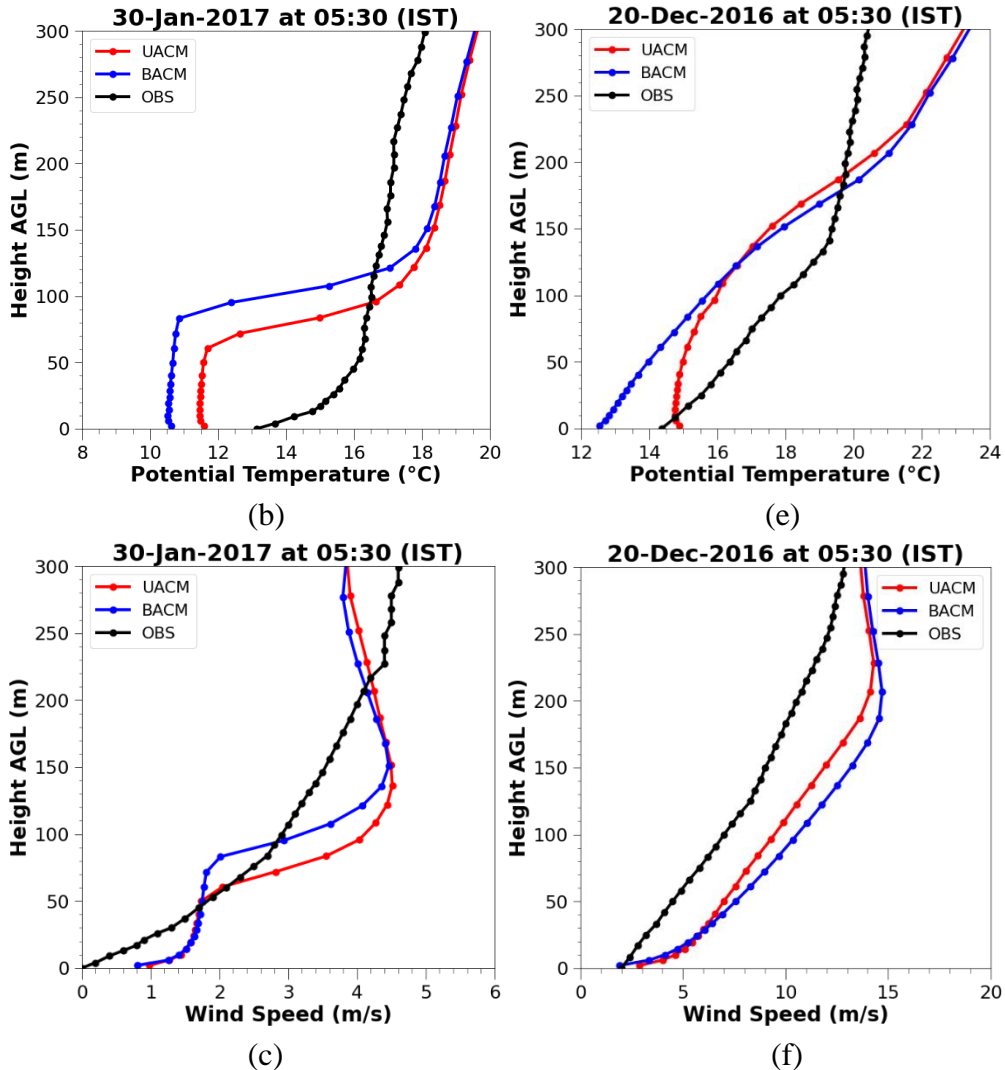
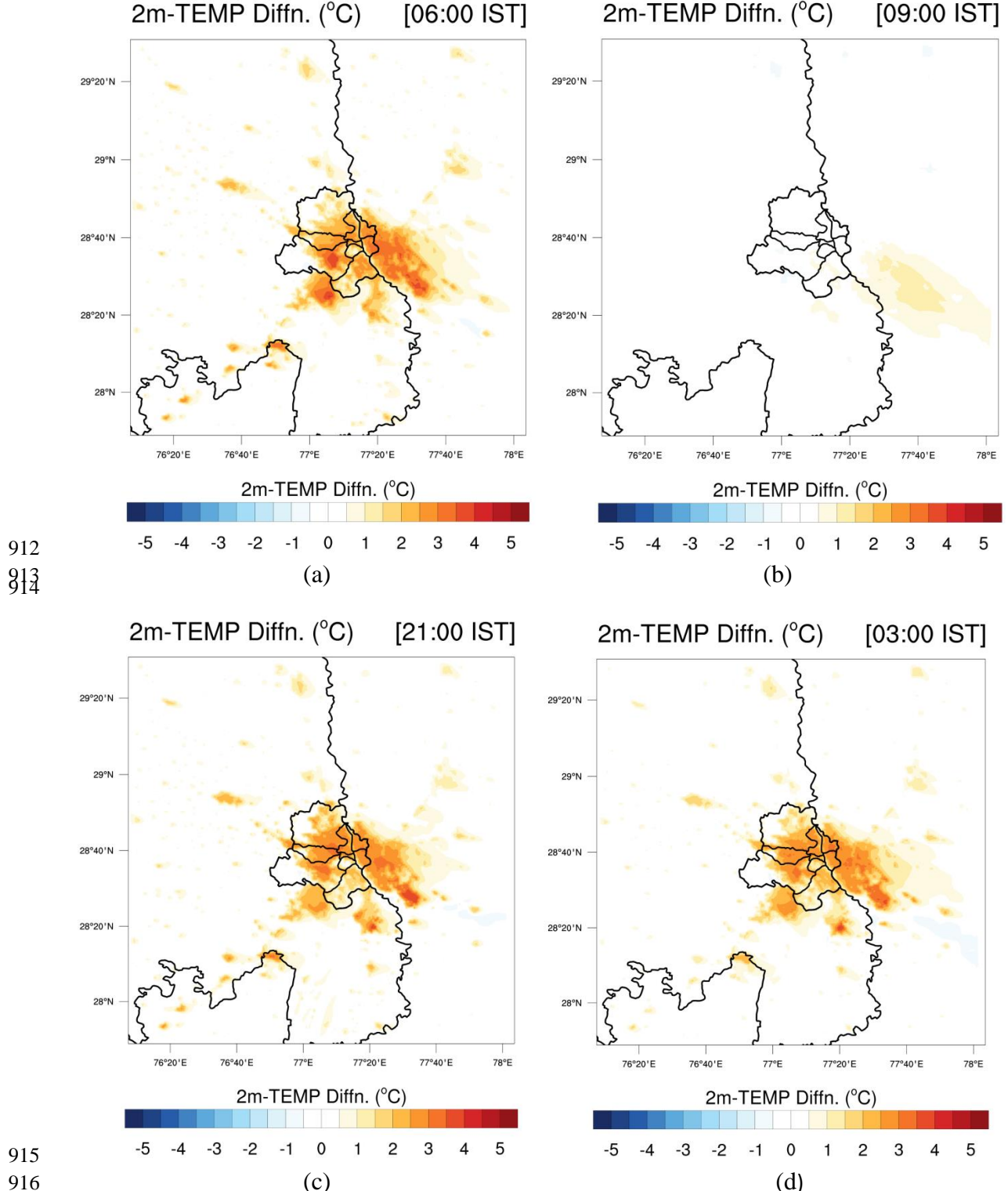
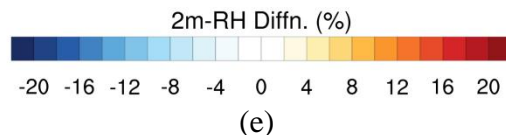
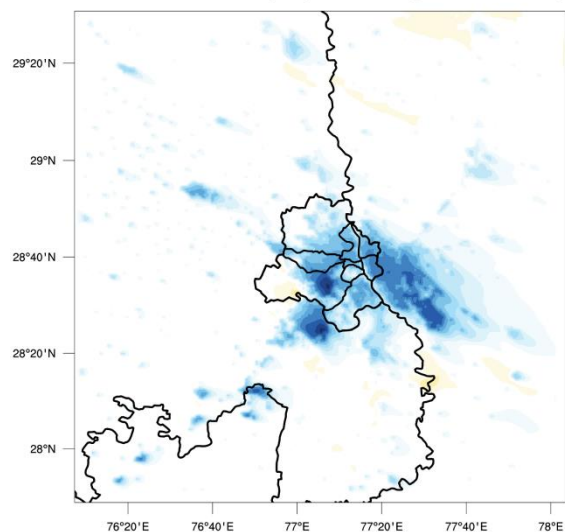


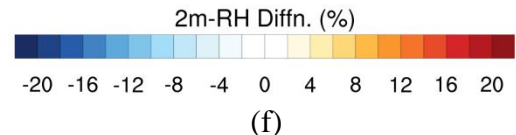
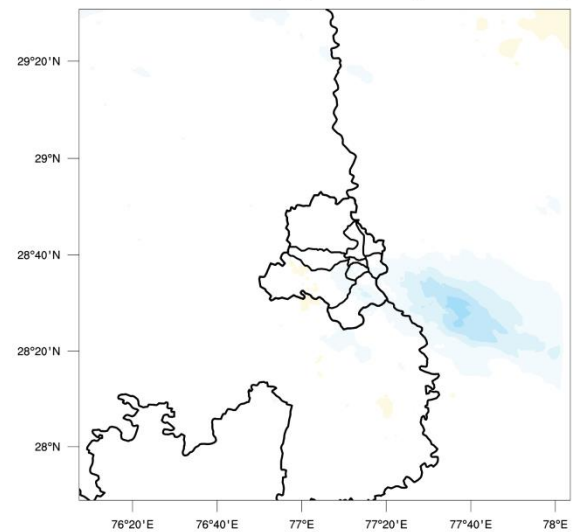
**Figure 6.** Vertical profiles of (a) relative humidity, (b) potential temperature, (c) horizontal wind speed on 30-Jan-2017 (05:30 IST) during a fog event case; and (d) relative humidity, (e) potential temperature, (f) horizontal wind speed on 20-Dec-2016 (05:30 IST) during a clear sky case at Ayanagar meteorological (IMD) station. UACM: Urban Asymmetric Convective Model; BACM: Base Asymmetric Convective Model (WRF model control runs); OBS: Observations.



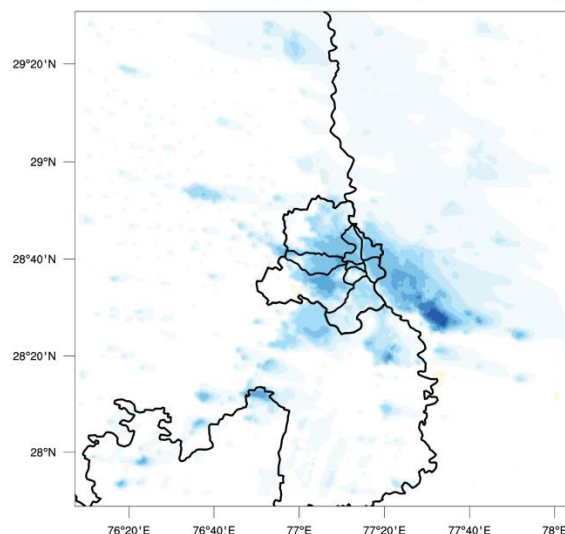
2m-RH Diffn. (%) [06:00 IST] 2m-RH Diffn. (%) [09:00 IST]



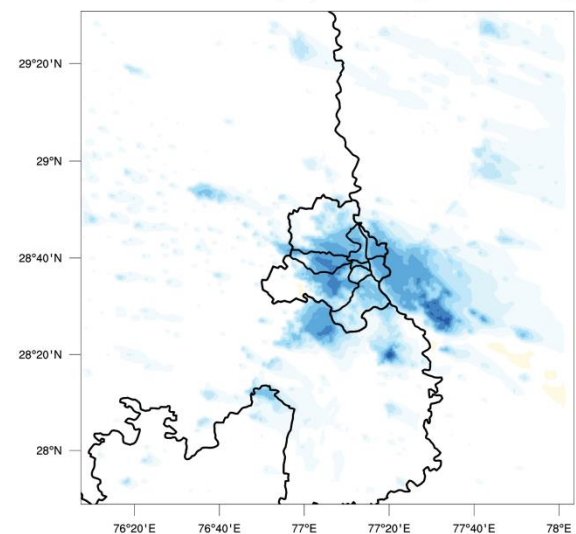
2m-RH Diffn. (%) [09:00 IST]



2m-RH Diffn. (%) [21:00 IST]



2m-RH Diffn. (%) [03:00 IST]



917  
918  
919

(e)

(f)

920  
921  
922

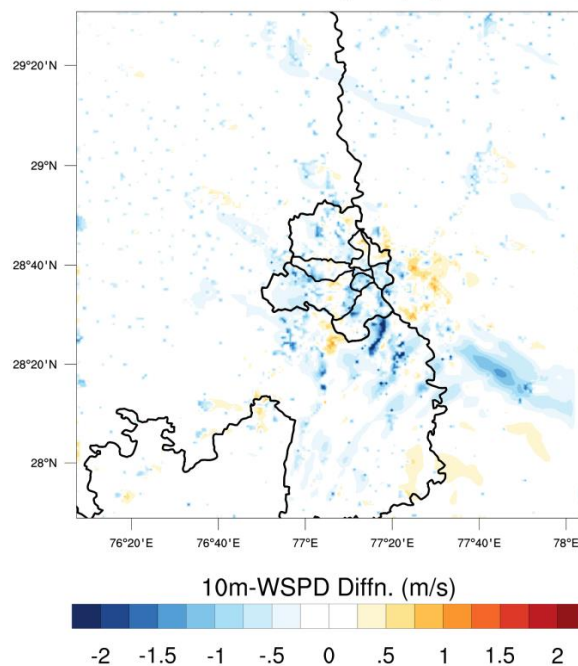
(g)

(h)

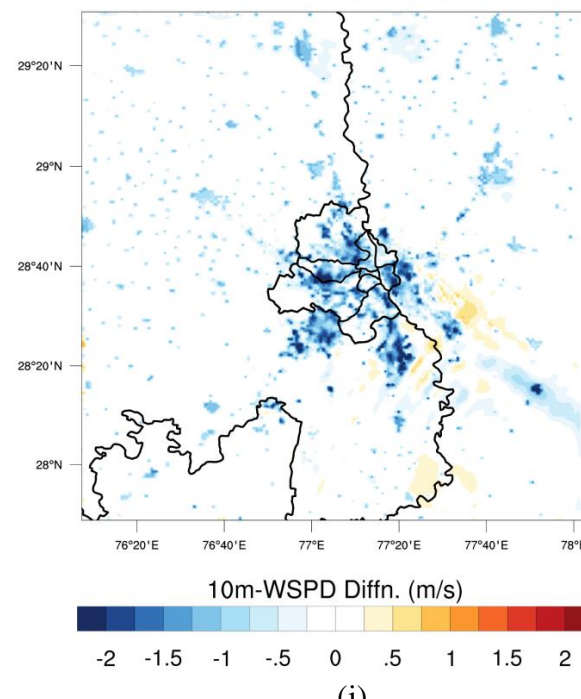
923  
924

925

10m-WSPD Diffn. (m/s) [06:00 IST]



10m-WSPD Diffn. (m/s) [09:00 IST]



926

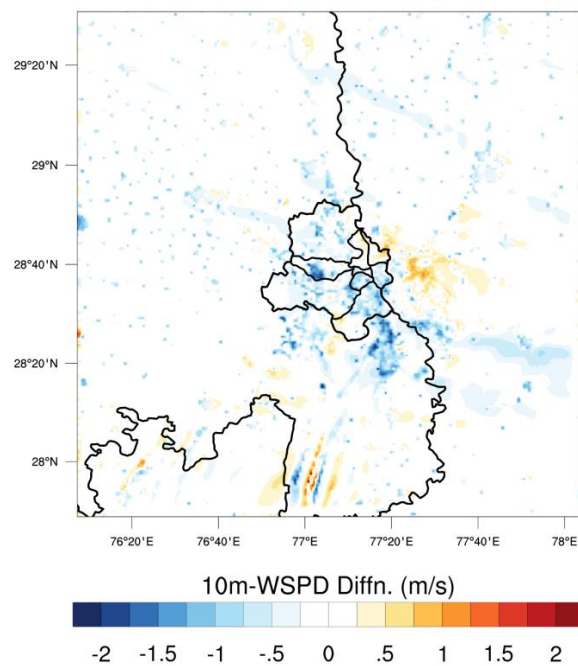
927

928

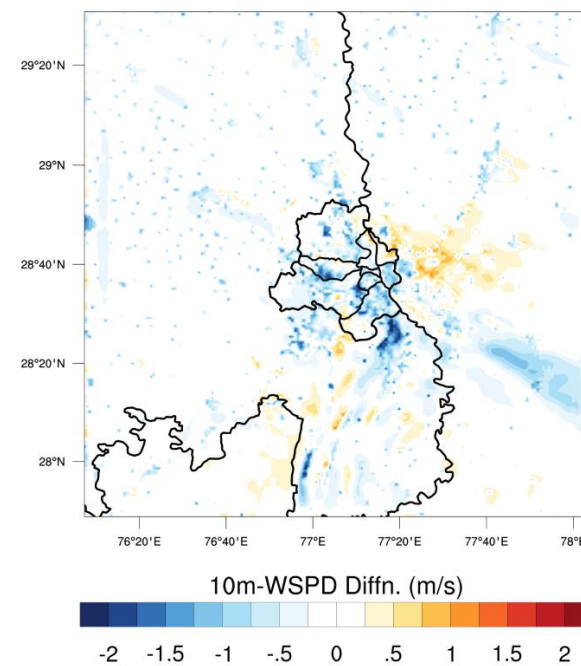
(i)

(j)

10m-WSPD Diffn. (m/s) [21:00 IST]



10m-WSPD Diffn. (m/s) [03:00 IST]



929

930

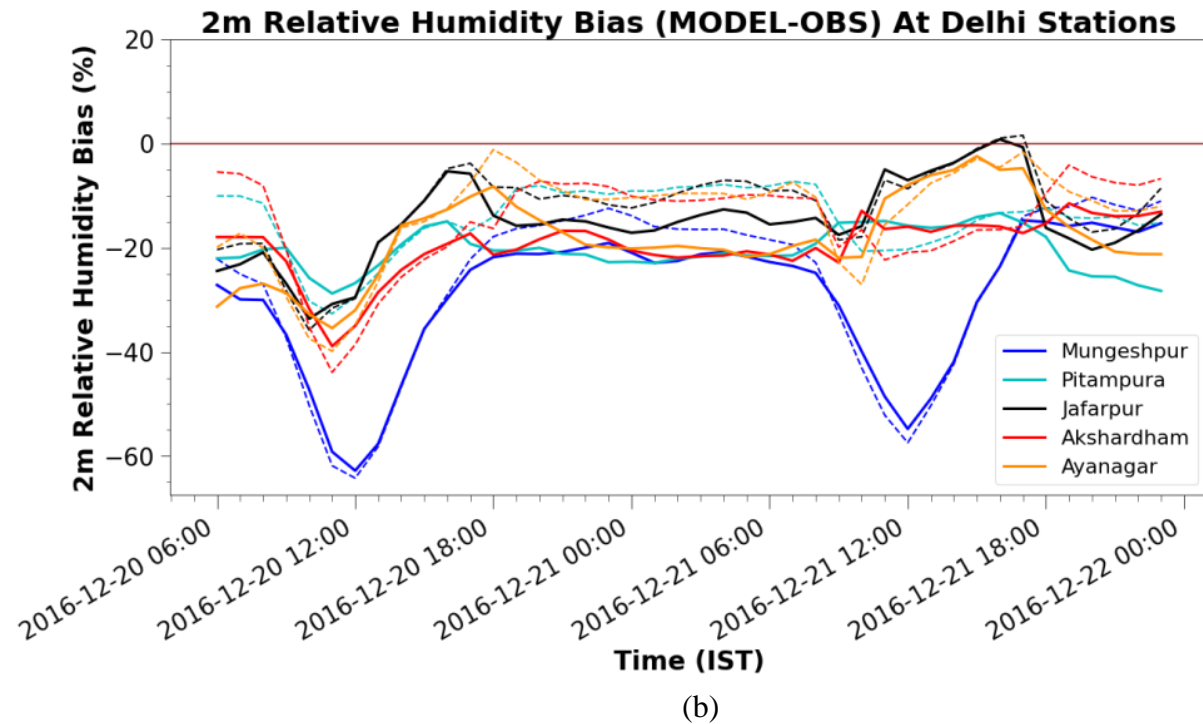
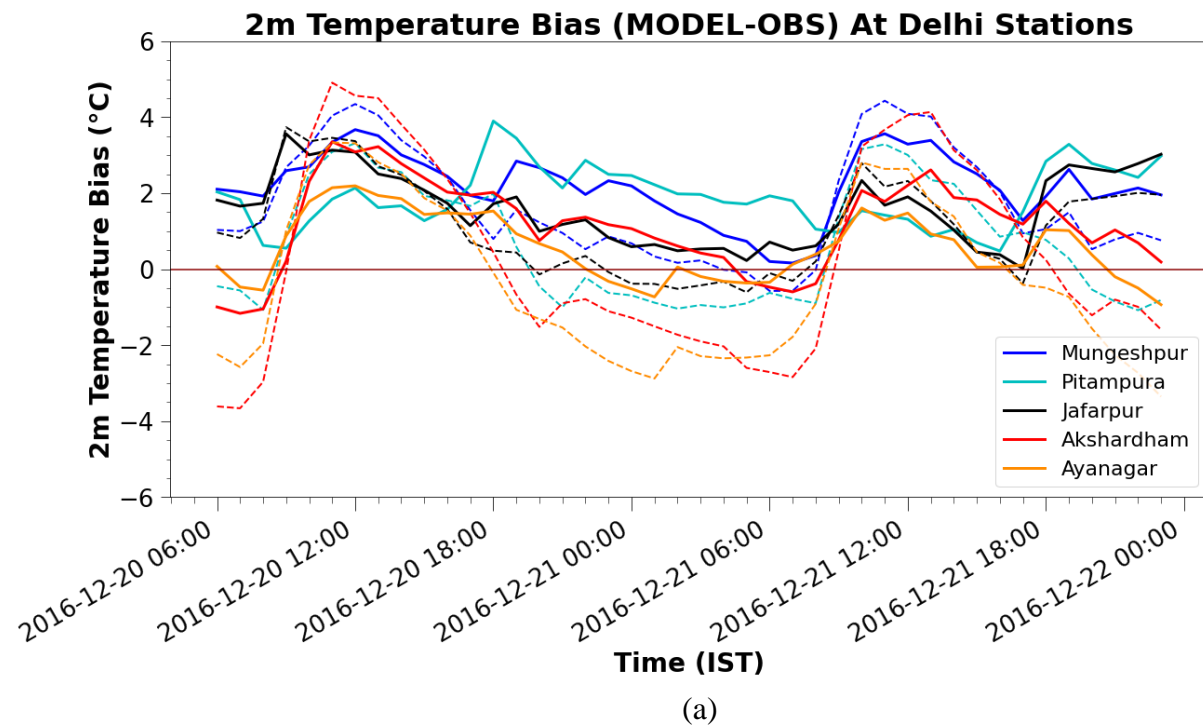
(k)

(l)

931      **Figure 7.** Contour plots of model difference [UACM – BACM] for (a-d) 2-m temperature, (e-h)  
 932      2-m relative humidity, and (i-l) 10-m wind speed during a clear sky case at 06:00 IST, 09:00 IST,  
 933      21:00 IST, and 03:00 IST on 20-Dec-2016.

934

935



938

939

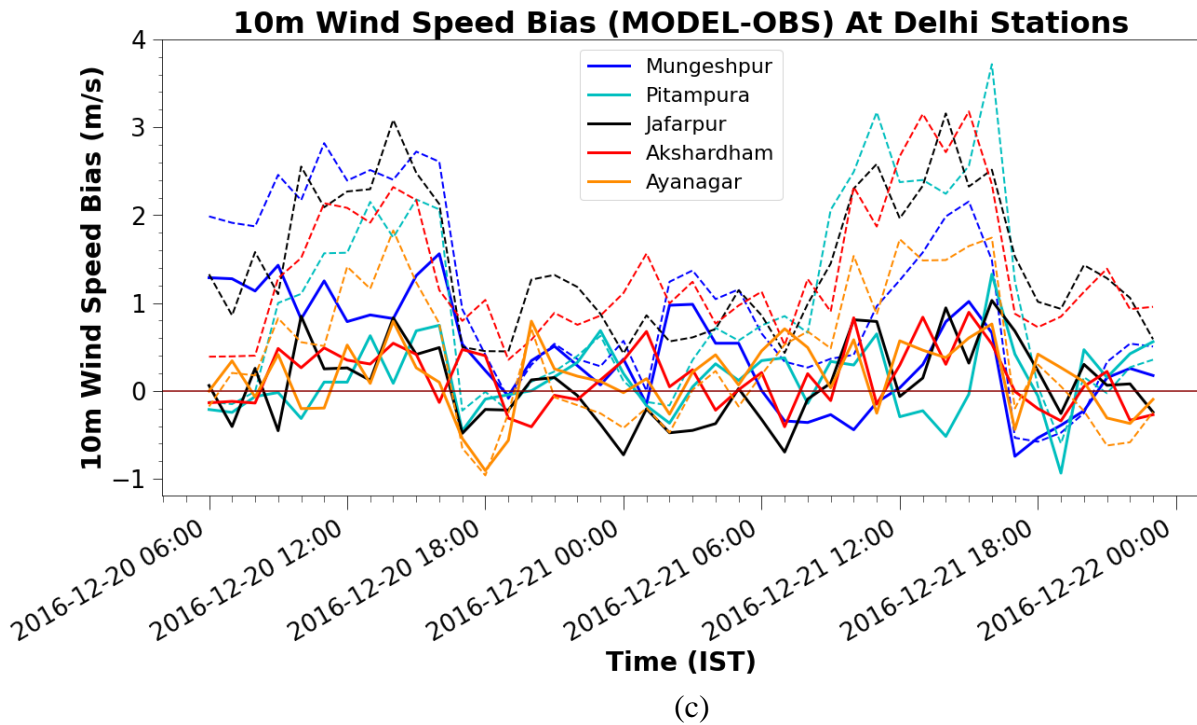


**Figure 8.** Time-series bias plots [MODEL – OBS] (bold line: UACM, dashed line: BACM) for (a) 2-m temperature, (b) 2-m relative humidity, (c) 10-m wind speed at Delhi urban Indian Meteorological Department (IMD) stations during a clear sky case from 20-Dec-2016 (06:00 IST) to 21-Dec-2016 (23:00 IST).

940  
941

942  
943  
944  
945

946

947

948

949

950

951

952

953

954

955

956 **Tables**

957

958 **Table 1.** Configuration settings used in the Weather Research and Forecasting (WRF) Model  
959 V3.8

<b>WRF V3.8 schemes and other options</b>	<b>Selected configuration</b>
Vertical sigma levels	54
Model top pressure	50 hPa (~20-km AGL)
Meteorological data (initial conditions)	National Centers for Environmental Prediction Final (Final Operational Global Analysis data) with a spatial resolution of 1° in latitude and longitude, and a temporal resolution of 6 h
Nested domain grid spacing	D1 (5 km), D2 (1 km)
Domain grid points	D1 (440 × 200), D2 (191 × 191)
Microphysics	WRF single-moment 6-class [WSM6] graupel scheme (D1-D2)
Longwave radiation	CAM LW scheme (D1-D2)
Shortwave radiation	CAM SW scheme (D1-D2)
Surface clay physics	Pleim-Xiu (PX) (D1-D2)
Surface physics	Pleim-Xiu (PX) scheme (D1), New Urban-PX scheme only at D2
Planetary boundary layer physics	Base-ACM2 (Pleim) scheme (D1) [BACM], New Urban-ACM2 [UACM] scheme only at D2
Cumulus physics	OFF (D1-D2)
No. of soil layers	2 (for PX)
No. of land categories	24 (USGS)
Nesting	One-way nesting
Coarse domain time step	8 s (with 1:4 parent time-step ratio)
No. of metgrid levels	27
No. of metgrid soil levels	4
Surface urban physics	OFF (D1-D2)

960 Note: ACM2 = Asymmetric Convective Model Version-2; BACM = Base Asymmetric  
961 Convective Model; UACM = Urban Asymmetric Convective Model.  
962  
963  
964  
965

966      **Table 2.** Statistical Metrics for 10-m Wind Speed, 2-m Temperature, and 2-m Relative Humidity  
 967      for a fog and clear sky case.

		10-m Wind Speed		2-m Temperature		2-m Relative Humidity	
		BACM	UACM	BACM	UACM	BACM	UACM
<b>Fog Event Case [29-30 January 2017]</b>	<b>IOA</b>	0.76	<b>0.89</b>	0.9	<b>0.96</b>	0.91	<b>0.92</b>
	<b>MB</b>	0.52	<b>0.14</b>	-1.03	<b>0.13</b>	<b>-1.32</b>	-6.62
	<b>NMB</b>	0.38	<b>0.09</b>	-0.06	<b>0.009</b>	<b>-0.01</b>	-0.07
	<b>ME</b>	0.69	<b>0.36</b>	2.0	<b>1.17</b>	<b>6.62</b>	7.49
	<b>NME</b>	0.48	<b>0.24</b>	0.13	<b>0.07</b>	<b>0.07</b>	0.08
	<b>RMSE</b>	0.9	<b>0.46</b>	2.29	<b>1.41</b>	<b>9.21</b>	9.33
<b>Clear Sky Case [20-22 Dec 2016]</b>	<b>IOA</b>	0.62	<b>0.88</b>	0.93	<b>0.94</b>	<b>0.76</b>	0.7
	<b>MB</b>	1.04	<b>0.18</b>	<b>0.7</b>	1.48	<b>-16.57</b>	-20.5
	<b>NMB</b>	0.33	<b>0.05</b>	<b>0.04</b>	0.08	<b>-0.24</b>	-0.3
	<b>ME</b>	1.13	<b>0.38</b>	1.7	<b>1.58</b>	<b>16.6</b>	20.5
	<b>NME</b>	0.35	<b>0.11</b>	0.1	<b>0.09</b>	<b>0.24</b>	0.3
	<b>RMSE</b>	1.39	<b>0.48</b>	2.05	<b>1.79</b>	<b>19.25</b>	22.1

968      Note: BACM = Base Asymmetric Convective Model; UACM = Urban Asymmetric Convective  
 969      Model; IOA = Index of Agreement; MB = Mean Bias; NMB = Normalized MB; ME = Mean  
 970      Error, NME = Normalized ME; RMSE = Room-Mean-Square Error.

971

972

973